AD-A286 177 ATION PAGE

1. Agency Use Only *(Leave blank).*	2. Report Date. September 1994	3. Report Type and Dates Covered. Journal Article

4. Title and Subtitle.
Response of a general circulation model to a change in cloud solar forcing: Model feedbacks and comparison with satellite data

5. Funding Numbers.
PE 0601153N
PN 3303-370
AN DN252021

6. Author(s).
James A. Ridout, NRL Monterey CA
Beth Chertock, NOAA ETL, Boulder CO
Ronald Gelaro, NRL Monterey CA

7. Performing Organization Name(s) and Address(es).
Naval Research Laboratory, Marine Meteorology Division
Monterey, CA 93943-5502

NOAA Environmental Technology Lab, Boulder, CO 80302

8. Performing Organization Report Number.

NRL/JA/7532--93-0011

9. Sponsoring/Monitoring Agency Name(s) and Address(es).

Office of Naval Research
Washington, DC 20375-5320

10. Sponsoring/Monitoring Agency Report Number.

12a. Distribution/Availability Statement.

Approved for public release; distribution unlimited.

12b. Distribution Code.

13. Abstract *(Maximum 200 words).*

The response of a general circulation model to a change in its treatment of cloud solar forcing is investigated. Radiation field data from the forecast model of the Navy Operational Global Atmospheric Prediction System for five Julys (1979-1983) are presented in an investigation of the effect of a change from grid cell averaged clouds to maximally overlapping clouds in the model's solar radiation scheme. The model results are compared with Nimbus 7 Earth Radiation Budget top of the atmosphere (TOA) solar and longwave irradiances and with derived surface irradiance data. Although the maximal overlap scheme performs considerably better than the grid cell averaging scheme (reducing maximum deficiencies in TOA and surface solar irradiance by over 100 W m^{-2}), significant errors remain. The simulated correlation between TOA net solar and longwave irradiance improves at low latitudes in the northern hemisphere, with little change at higher latitudes. (... continues ...)

14. Subject Terms. General circulation model Cloud radiative heating Cloud solar forcing	15. Number of Pages. 22
	16. Price Code.

17. Security Classification of Report. UNCLASSIFIED	18. Security Classification of This Page. UNCLASSIFIED	19. Security Classification of Abstract. UNCLASSIFIED	20. Limitation of Abstract. UNLIMITED

Response of a general circulation model to a change in cloud solar forcing: Model feedbacks and comparison with satellite data

James A. Ridout

Naval Research Laboratory, Monterey, California

Beth Chertock

National Oceanic and Atmospheric Administration, Environmental Technology Laboratory, Boulder, Colorado

Ronald Gelaro

Naval Research Laboratory, Monterey, California

Abstract. The response of a general circulation model to a change in its treatment of cloud solar forcing is investigated. Radiation field data from the forecast model of the Navy Operational Global Atmospheric Prediction System for five Julys (1979–1983) are presented in an investigation of the effect of a change from grid cell averaged clouds to maximally overlapping clouds in the model's solar radiation scheme. The model results are compared with Nimbus 7 Earth Radiation Budget top of the atmosphere (TOA) solar and longwave irradiances and with derived surface solar irradiance data. Although the maximal overlap scheme performs considerably better than the grid cell averaging scheme (reducing maximum deficiencies in TOA and surface solar irradiance by over 100 W m^{-2}), significant errors remain. The simulated correlation between TOA net solar and longwave irradiance improves at low latitudes in the northern hemisphere, with little change at higher latitudes. This improved correlation is consistent with the greater consistency between the treatments of solar and longwave cloud radiative forcing brought to the model by the new solar radiation scheme. The change in the radiation treatment is shown to have the greatest direct effect on solar radiation over convective regions, a consequence of the scarcity of optically thick clouds produced by the model's cloud parameterization in other regions. The model responds with an increase in convective activity over land and an increase in the flux of moisture from sea to land. Planetary cooling over the oceans increases because of a decrease in cloud cover. From mid to high latitudes in the northern hemisphere, there are scattered regions of increased cloud water content associated with increased tropospheric temperatures. Over land the model response in terms of TOA downwelling solar irradiance tends to counter the increase in solar irradiance caused by the model change in all latitudinal zones in the northern hemisphere. This response is caused primarily by changes in the cloud fields, which thus act as a negative feedback following the change in cloud solar forcing. The significance of this response is examined with respect to the perturbation in solar irradiance represented by the model change. An estimate of this perturbation is obtained by taking the difference in solar irradiance diagnosed by the two cloud solar forcing treatments for simulations employing the grid cell averaging scheme. The response is significantly greater in magnitude in the tropics than at midlatitudes, both in an absolute sense and as a percentage of this perturbation. Because TOA longwave irradiance exhibits a positive response in the tropics, and a negative response at midlatitudes, however, the percentage response in net TOA downwelling irradiance is actually greater in magnitude at midlatitudes. In a number of regions the cloud feedback is very large, showing the importance for cloud field prediction of improvements in the treatment of cloud solar forcing. Such cloud feedback also explains the small improvement seen here in the prediction of TOA solar irradiance in certain regions. Increases in surface sensible heating and longwave cooling are generally considerably less than increases in surface latent heating, though a notable exception occurs in arid central Asia. A large

DTIC QUALITY INSPECTED 1

94 11 10 002

ground temperature increase in that region is strongly correlated at low levels with the atmospheric temperature increase observed at midlatitudes in the northern hemisphere.

1. Introduction

The importance of clouds in modulating the radiative heating of the Earth-atmosphere system has stimulated a substantial amount of research into cloud radiative effects in recent years. Research on global-scale cloud radiative effects has included both observational studies [e.g., *London*, 1957; *Budyko*, 1969; *Cess*, 1976; *Ohring and Clapp*, 1980; *Ramanathan et al.*, 1989; *Ardanuy et al.*, 1991; *Smith and Vonder Haar*, 1991; *Hartmann et al.*, 1992; *Laszlo and Pinker*, 1993] and modeling studies [e.g., *Cess and Potter*, 1987; *Slingo and Slingo*, 1988; *Harshvardhan et al.*, 1989; *Cess et al.*, 1990; *Morcrette*, 1990; *Slingo and Slingo*, 1991; *Potter et al.*, 1992]. To gain insight into how model accuracy can be improved, a growing number of studies have compared model radiation fields with satellite observations or with satellite-derived data [e.g., *Geleyn et al.*, 1982; *Slingo et al.*, 1987; *Buriez et al.*, 1988; *Kiehl and Ramanathan*, 1990; *Bony et al.*, 1992; *Chertock and Sud*, 1993].

Because of the complex nature of clouds number of uncertainties are generally associated with modeling studies of cloud radiative properties. Variations in the microphysical structure of clouds can affect cloud radiative properties tremendously [e.g., *Wiscombe et al.*, 1984; *Ackerman and Stephens*, 1987; *Liou et al.*, 1991], as can variations in cloud cover, cloud macrophysical shape, and the spatial distribution of water in clouds [e.g., *McKee and Cox*, 1974; *Aida*, 1976; *Davies*, 1978; *Weinman and Harshvardhan*, 1982; *Harshvardhan*, 1982; *Welch and Wielicki*, 1984; *Kite*, 1987]. The complex nature of clouds is particularly problematic for attempts to simulate their effect on the large-scale circulation. General circulation models (GCMs) are constrained at present to using only very crude treatments of clouds and their radiative interactions. In such models, cloud properties are often parameterized in terms of large-scale variables, though explicit schemes that carry a prognostic variable for cloud water have also been developed [e.g., *Smith*, 1990]. In the diagnostic schemes, cloud amount is assumed to depend on such quantities as large-scale relative humidity, convective precipitation, vertical potential temperature gradient, and vertical velocity [e.g., *Slingo*, 1987]. Radiative transfer in cloudy grid cells is generally treated using calculations that are based, at least to some degree, on the (plane-parallel) assumption that clouds, and hence radiation fields, do not vary at all in the horizontal.

Our work examines the effects of a change from the use of grid cell averaged clouds to maximally overlapping clouds in the solar radiation scheme of the spectral forecast model of the Navy Operational Global Atmospheric Prediction System (NOGAPS). The assumption of maximal cloud overlap is employed in the model's longwave radiation scheme [*Harshvardhan et al.*, 1987] but has not previously been used in the NOGAPS solar radiation scheme, where it is potentially considerably more computer intensive than the grid cell averaging treatment currently used. Further discussion of the NOGAPS GCM is given in section 2, along with a discussion of the simulations that were used for the present work. In the first part of our study the model results are compared with Nimbus 7 Earth Radiation Budget (ERB)

observations in order to assess the net effect of the change in cloud solar forcing with respect to observed model errors. This comparison is presented in section 4, following a discussion in section 3 of the radiation data that are used. Both the direct effect of the change in the treatment of cloud solar forcing and the model response to that change in terms of radiation fields are examined in section 5. In section 6 the response of model cloud fields is examined. Changes in precipitation and ground and atmospheric temperatures are discussed in section 7.

2. Model and Simulation Details

Simulation data from version 3.3 of the NOGAPS forecast model (NOGAPS 3.3), taken from a 10-year simulation beginning January 1979, were used for this work. This simulation was carried out at the Naval Research Laboratory (NRL) as part of the Program for Climate Model Diagnosis and Intercomparison (PCMDI). Data from simulations for the five consecutive Julys beginning in 1979, carried out with a maximal overlap version of the NOGAPS model, described below, were also used. Fields from the NOGAPS 3.3 PCMDI simulations were used to initialize the model for these simulations, and a 1-month spin-up period was used for each simulation.

Version 3.3 of the NOGAPS forecast model is a spectral model with 18 vertical levels. This model was implemented for the PCMDI simulations with a triangular truncation at wavenumber 47, which corresponds roughly to a 2.5° transform grid. The radiation scheme is that of *Davies* [1982] and *Harshvardhan et al.* [1987], the solar portion of which is an extension of the scheme developed by *Lacis and Hansen* [1974]. The only gases assumed to be absorbers of solar radiation are water vapor and ozone, and the effects of aerosols are ignored. The cloud scheme is similar to the diagnostic parameterization of *Slingo* [1987]. The prediction of convective clouds differs from that of Slingo, however, in that convective precipitation at the surface is used to diagnose convective cloud cover, rather than the precipitation at cloud base level. More detailed descriptions of the model are given by *Hogan and Rosmond* [1991], who present a discussion of NOGAPS 3.2, and by *Hogan and Brody* [1993], who list changes incorporated into version 3.3 of NOGAPS. These changes include the adoption of the assumption of maximally overlapping clouds in the model's treatment of longwave radiation and the change to a more realistic value of single scatter albedo for radiative transfer of solar radiation in clouds. The parameterization of cloud optical thickness that was used for the PCMDI simulations is also a new feature of the model. The present parameterization was developed by Tim Hogan at NRL and is described in the appendix. Although this parameterization appears to produce optical thicknesses that are too low in the case of convective clouds, and will tend to reduce to some extent differences between the two radiation schemes examined here, this fact should not significantly affect the results of our present study.

Where partial cloudiness occurs, the treatment of longwave radiation in NOGAPS 3.3 follows the maximal overlap

treatment described by *Harshvardhan et al.* [1987]. There is no provision in the Harshvardhan et al. radiation scheme, however, for a similar treatment of solar radiation. In the solar radiation scheme, partially cloudy grid cells are treated using a grid cell averaging treatment in which the optical thickness of clouds is obtained by averaging cloud optical thickness over the entire grid cell. This was not much of a problem in the University of California, Los Angeles/Goddard Laboratory for Atmospheres (UCLA)/GLA GCM for which the Harshvardhan et al. scheme was designed, because partial cloudiness was allowed only for optically thin boundary layer clouds [*Harshvardhan et al.*, 1989]. In NOGA PS 3.3, however, the inconsistency between the treatment of partial cloudiness used for solar radiation and that used for longwave radiation is potentially of considerable consequence. We found that this inconsistency can be avoided in an economical manner by repeated application of the Harshvardhan et al. scheme. In this treatment, solar irradiances are summed for each different vertical profile of cloudiness in a given grid column consistent with the assumption of maximal cloud overlap (see Figure 1). The revised model in which this maximal overlap treatment is used for solar radiation, denoted here as NOGAPS 3.3MO, requires only about 10% more CPU time on a CRAY Y-MP than does NOGAPS 3.3.

3. Radiation Data

The model simulation results were compared with July mean top of the atmosphere (TOA) net downwelling solar and outgoing longwave irradiances for the years 1979–1983 derived from wide-angle field-of-view (WFOV) Nimbus 7 ERB Experiment observations [*Jacobowitz et al.*, 1984; *Kyle et al.*, 1985] and with corresponding July mean surface solar irradiances over the oceans derived from Nimbus 7 ERB planetary albedo data by *Chertock et al.* [1992] using the model of *Chertock* [1989] and *Frouin and Chertock* [1992]. These data are based on observations from a single Sun-synchronous satellite, which means that modeled diurnal cycles of albedo and outgoing longwave radiation had to be used to produce the monthly mean data. It has been shown, however, that the ERB TOA data compare favorably with Earth Radiation Budget Experiment (ERBE) data derived from observations from a trio of sun-synchronous satellites: ERBS, NOAA 9, and NOAA 10 [*Kyle et al.*, 1990]. The RMS differences between WFOV ERB and ERBE data interpolated to the higher-resolution 2.5° grid of the ERBE scanner data for April and July 1985 are approximately 4 W m^{-2} for longwave irradiances and 8–9 W m^{-2} for solar irradiances at the top of the atmosphere [*Kyle et al.*, 1990]. The RMS differences between the WFOV ERB data and the ERBE scanner data for the same months and grid are approximately 10 W m^{-2} for longwave irradiances and 14–15 W m^{-2} for solar irradiances. Although the level taken to be the TOA in processing the ERB data was somewhat arbitrarily taken to be 15 km above sea level, it has been shown that raising this level to 30 km above sea level produces only a fraction of a percent difference in calculated WFOV longwave irradiances [*Kyle et al.*, 1990]. The surface solar irradiance data used here have been estimated to be accurate to within 10–20 W m^{-2} for monthly averages at the 9° grid resolution of the present study [*Chertock et al.*, 1992].

The availability of data near the poles varied. TOA net
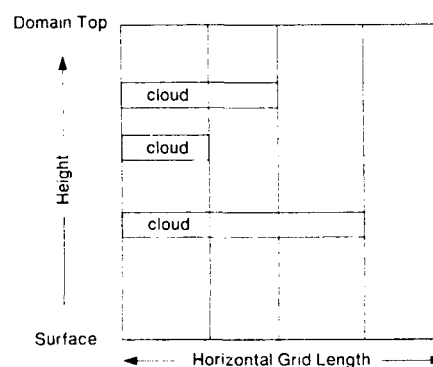
Figure 1. Vertical cross section through a model grid column. The maximal overlap assumption is implemented for the hypothetical cloudiness profile shown here by applying the model's radiation scheme separately to each of the four indicated vertical columns.

solar irradiances (obtained from albedo and insolation data) were available between 72°S and 72°N for the five Julys. The same was generally true of outgoing longwave irradiances, except for July 1980, for which data were not available poleward of 54°N. The surface solar irradiance data were available between 63°S and 63°N.

4. Error in Model Radiation Fields

4.1. Solar Radiation Comparisons

The mean TOA net downwelling solar irradiance observed from ERB data for the five consecutive Julys is shown in Figure 2a. The difference between the corresponding values obtained with the models and the observed values is shown in Figure 2b for NOGAPS 3.3 and in Figure 2c for NOGAPS 3.3MO. Such differences will be referred to hereinafter as errors, though they are not necessarily true errors because of inaccuracies in the ERB and derived surface solar irradiance data. Shading is used here, and in all our difference maps, to indicate where the Student's t test assigns a significance to the plotted mean differences, scaled with the pooled monthly variability of these means, at the 95% level. The results in Figure 2 show a striking improvement with the maximal overlap scheme, though substantial errors still exist. Over the Pacific Ocean, for example, the maximum deficiency of TOA net solar irradiance obtained with the NOGAPS model is reduced from 172 W m^{-2} to 49 W m^{-2} with the new scheme. Both model versions produce large errors over the Indian Ocean, though NOGAPS 3.3MO does somewhat better. The peak deficiency in that region is reduced from 152 W m^{-2} to 91 W m^{-2} with the maximal overlap scheme.

The results in Figure 2 show a large amount of regional variability in the differences between the grid cell averaging and the maximal overlap treatments. In order to better understand the observed differences, we show in Figure 3a the mean surface convective rainfall rate from the NOGAPS 3.3 simulations for the five Julys. A comparison of the convective rainfall shown in Figure 3a with the TOA solar irradiance error shown in Figure 2b indicates a strong correlation between simulated convective rainfall and deficiencies in TOA net solar irradiance predicted by the cloud grid cell averaging scheme of NOGAPS 3.3. In Figure 3b, which shows the differences between the convective rainfall
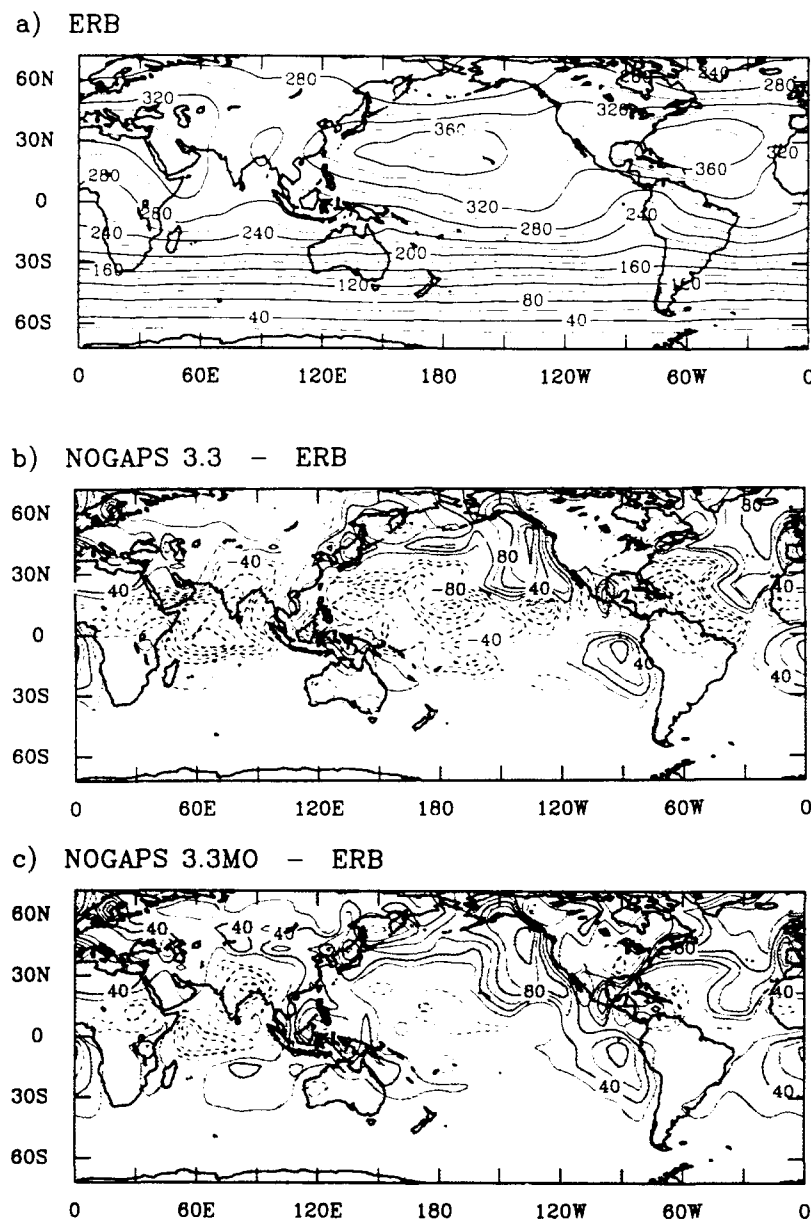
Figure 2. (a) July mean TOA net solar irradiance (in watts per square meter) from ERB measurements. (b) difference between results from NOGAPS 3.3 and the data shown in Figure 2a, and (c) difference between results from NOGAPS 3.3MO and the data shown in Figure 2a. Shaded regions are those for which the plotted differences are statistically significant at the 95% level according to the results of a Student's t test. The contour interval is 20 W m^{-2}, and the zero contour has been omitted. Negative contours are indicated by dashed lines.

rates predicted by the two model versions, we see that although there are some significant fractional increases in convective rainfall over land, particularly over Africa and North and South America, differences in convective activity do not explain the large differences between Figures 2a and 2b. The increased convection obtained with NOGAPS 3.3MO over land should, in fact, tend to increase the deficiencies in TOA solar irradiance, but this is not observed. The correlation between the error in Figure 2b and the convective rainfall simulated by NOGAPS 3.3 appears to stem, rather, from the optically thick clouds parameterized in regions of deep convection by the cloud parameterization scheme used in the NOGAPS model. For water clouds,

optical thickness is assumed to be proportional to the saturation specific humidity, and it is the relatively low base levels of convective clouds that are most responsible for their significant optical thickness in the NOGAPS simulations. The poor performance of the grid cell averaging scheme for convective clouds most likely stems from the well-known fact that for optically thick plane-parallel clouds, albedos asymptotically approach a limiting value [e.g.. Chandrasekhar, 1960, pp. 89–91; Arking and Childs, 1985; Stephens and Tsay, 1990]. When one averages cloud optical thickness over model grid cells for optically thick clouds, the effect of the decrease in the albedo of the cloud-covered region can be small in comparison with the net increase in

a)

b)
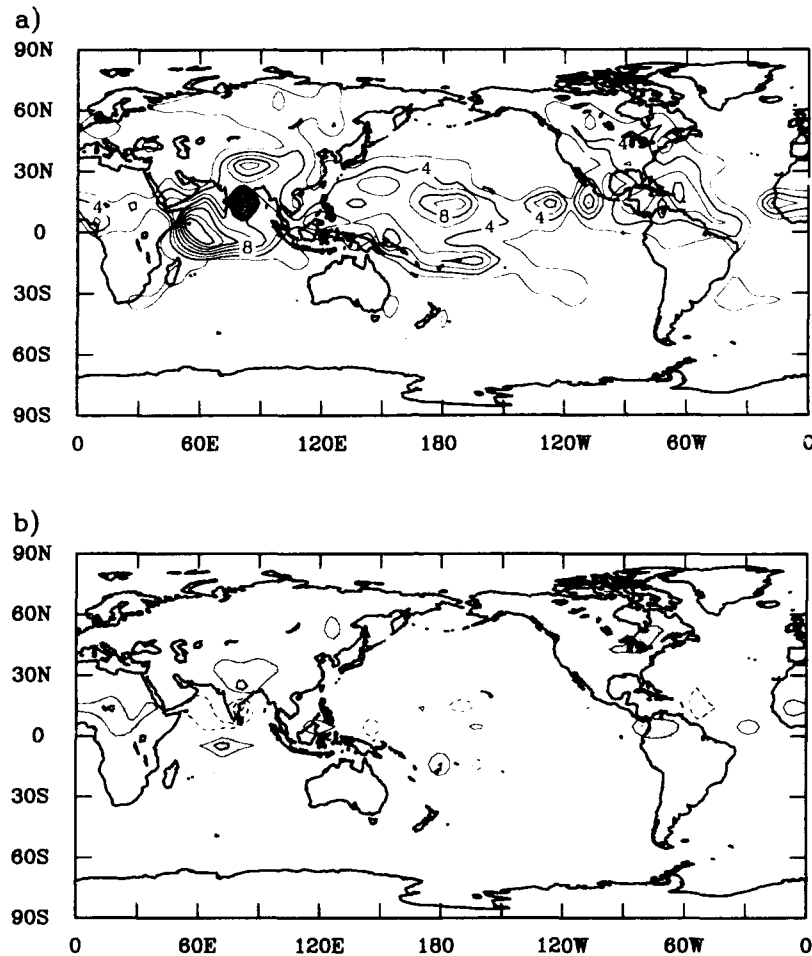
Figure 3. (a) July mean surface convective precipitation rate (in millimeters per day) predicted by NOGAPS 3.3 and (b) the difference between the corresponding results obtained with NOGAPS 3.3MO and the results obtained with NOGAPS 3.3. The contour interval is 2 mm d^{-1}. Shading is defined as in Figure 2.

the grid-scale albedo that results from having a greater area covered by cloud. An illustration of this fact is shown in Figure 4, where the albedos obtained using the two cloud solar forcing schemes considered here for a cylindrical cloud
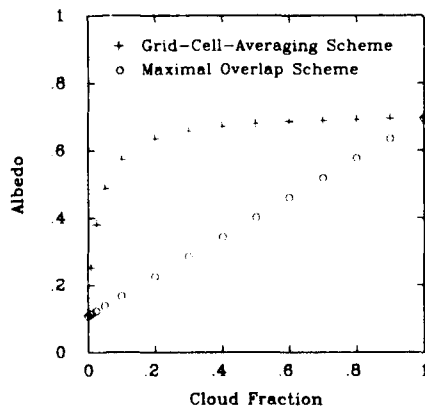
Figure 4. Albedo plotted against cloud fraction for a cylindrical cloud of an optical thickness of 328 that extends from 1.1 km above the surface to a height of 6.5 km.

of optical thickness equal to 328 that extends from 1.1 km above the surface to a height of 6.5 km are plotted as a function of cloud fraction. The results shown for the grid cell averaging scheme are the same as would be obtained for a cloud fraction of unity and a cloud optical thickness that is varied linearly from zero to 328. The grid cell averaging scheme thus produces an asymptotic dependence of albedo on cloud fraction that seems considerably less reasonable than the linear relationship obtained with the maximal overlap scheme.

Although the maximal overlap scheme in NOGAPS 3.3MO yields significantly improved results over regions of deep convection, significant errors remain, both in convective regions and elsewhere. We note here the model's tendency to predict excessively large values of TOA net solar irradiance over regions where extensive marine stratiform cloud coverage should occur. Where low-level stratus or stratocumulus clouds generally predominate in nature, a substantial portion of the model error apparently results from the fact that the model significantly underestimates the occurrence of such clouds [Hogan and Brody, 1993]. For July 1985, for example, NOGAPS predicts a cloud fraction of 0.1 (defined here to be the greatest cloud fraction at any

a) ERB

b) NOGAPS 3.3 — ERB
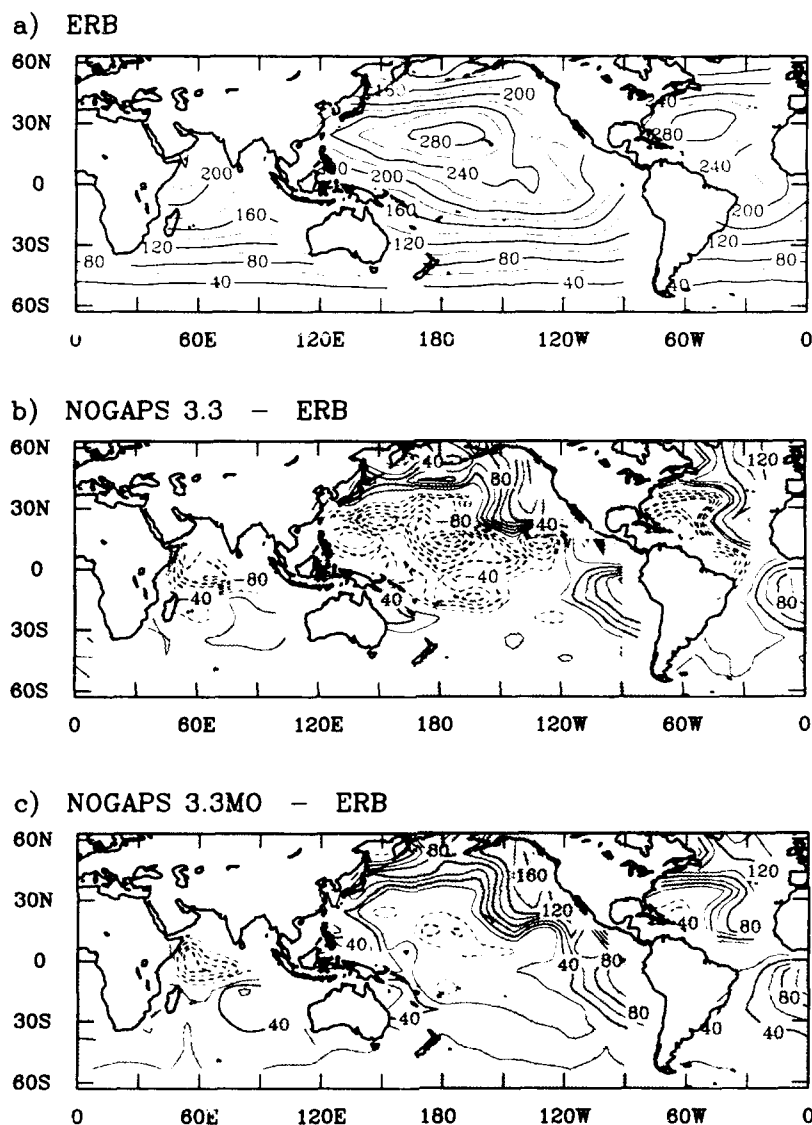
c) NOGAPS 3.3MO — ERB

Figure 5. (a) July mean surface solar irradiance (in watts per square meter) derived from ERB measurements, (b) difference between the results from NOGAPS 3.3 and the data shown in Figure 5a, and (c) difference between the results from NOGAPS 3.3MO and the data shown in Figure 5a. Shading and contours are defined as in Figure 2.

model grid level) for a 5° latitude (12.5°S to 17.5°S) by 7.5° longitude (80°W to 87.5°W) region off the west coast of South America known to be dominated by stratus clouds. For the same region and month, Ockert-Bell and Hartmann [1992] recently reported a low-level (below 680 mbar) cloud fraction of 0.6. Similar model deficiencies have been reported in some related model validation studies [Buriez et al., 1988; Vesperini et al., 1991; Soden, 1992]. The failure of NOGAPS in this regard stems from its requirement for an unrealistically strong low-level inversion for stratus clouds to occur (T. Rosmond, personal communication, 1993), a problem which has since been corrected.

The 5-year July mean surface solar irradiance data are presented in Figure 5a. The plotted values appear to be rather highly correlated with the values of TOA net downwelling solar irradiance plotted in Figure 2, as similarly noted by Laszlo and Pinker [1993]. The differences between the model predictions and the ERB-derived data are shown

in Figures 5b and 5c. Over regions of considerable convective activity the maximal overlap scheme yields a substantial improvement in predicted values of surface solar irradiance similar to that shown in Figure 2 for TOA solar irradiance. Peak deficiencies of 194 W m^{-2} and 96 W m^{-2} are obtained for NOGAPS 3.3 and NOGAPS 3.3MO, respectively; the former value occurred in the central Pacific Ocean, and the latter value occurred in the Indian Ocean. The deficiency of 194 W m^{-2} in the central Pacific obtained with NOGAPS 3.3 is reduced to 53 W m^{-2} in the NOGAPS 3.3MO simulations.

Comparisons of the model-generated zonal means of TOA net solar irradiance with ERB data are shown in Figure 6. Over many latitudinal zones, regional errors in NOGAPS 3.3 tend to compensate to produce reasonably accurate zonal means. Such is not the case over the northern hemisphere tropics, however, where large deficiencies of net solar irradiance exist. The revised model does not produce the sizable errors in tropical zonal means that characterize
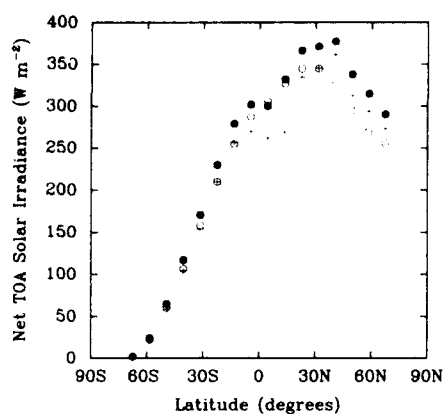
Figure 6. Zonal July mean TOA net solar irradiance. Results from NOGAPS 3.3 (plus signs), and NOGAPS 3.3MO (solid circles) are shown with ERB data (open circles).

NOGAPS 3.3, but it does exhibit a general tendency to overpredict the amount of net downwelling solar radiation, particularly for midlatitudinal and high-latitudinal zones of the northern hemisphere. Some of this error results from the failure of the model to predict enough low-level marine stratus clouds, as indicated in the discussion above. The fact that NOGAPS 3.3MO tends to err somewhat more on the high side than does NOGAPS 3.3 may well result from an inadequacy of the maximal overlap assumption for certain regions, though this conclusion cannot be positively deduced from our results.

4.2. Longwave Radiation Comparisons

A plot of mean TOA outgoing longwave irradiance obtained from the ERB Experiment for the five Julys is shown in Figure 7, together with plots of the difference between the model-derived values and the observations. The results indicate considerable errors in the longwave irradiance field

a) ERB

b) NOGAPS 3.3 — ERB
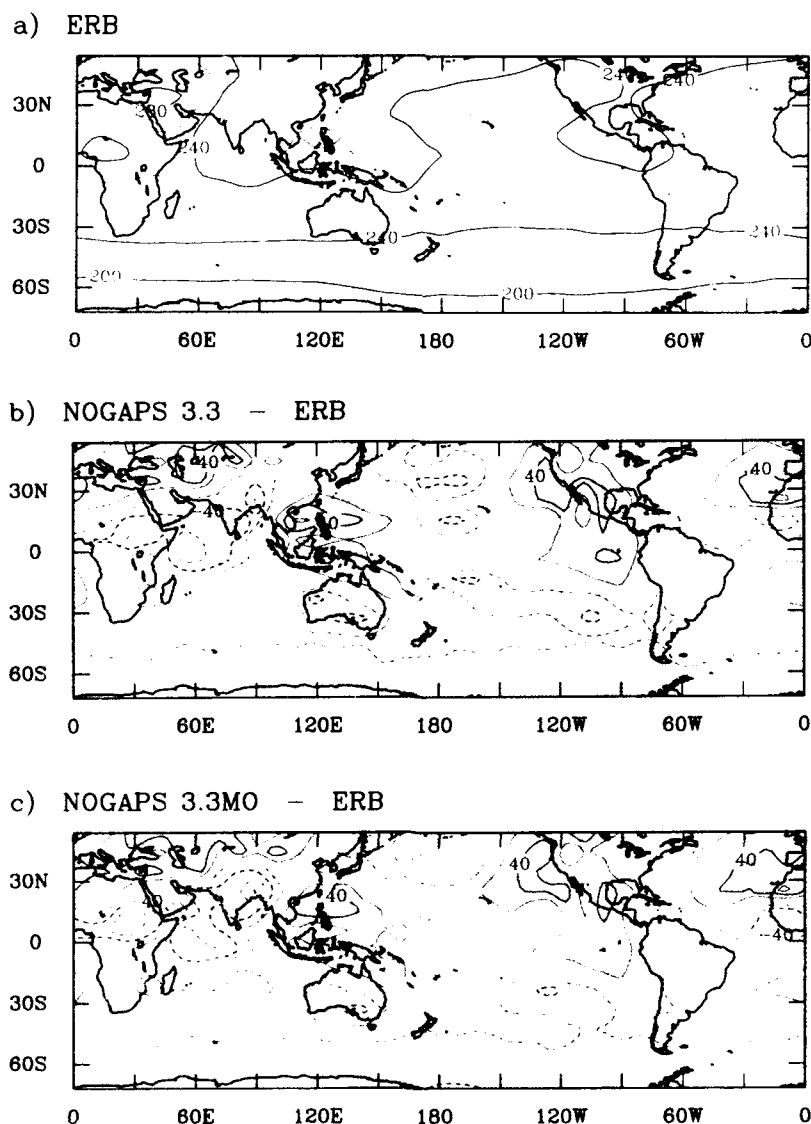
c) NOGAPS 3.3MO — ERB

Figure 7. (a) July mean TOA outgoing longwave irradiance (in watts per square meter) from ERB measurements, (b) difference between the results from NOGAPS 3.3 and the data shown in Figure 7a, and (c) difference between the results from NOGAPS 3.3MO and the data shown in Figure 7a. Shading and contours are defined as in Figure 2.

a)

b)
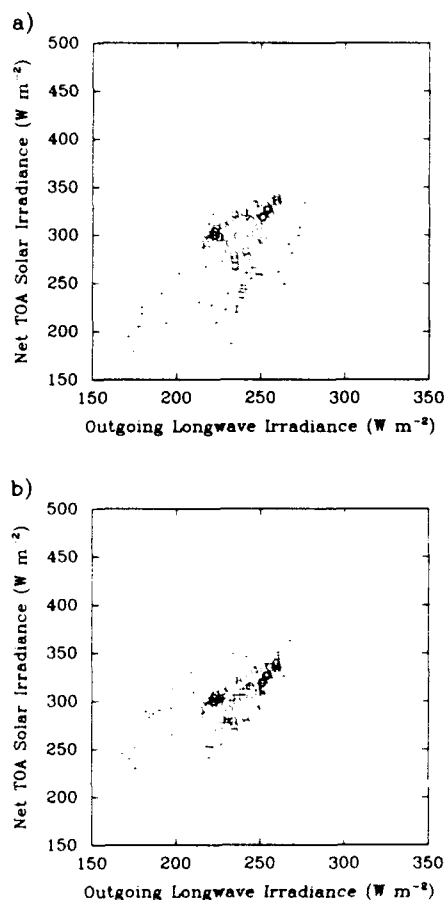
Figure 8. July mean TOA net solar irradiance for $9° \times 9°$ regions extending from $0°$ to $9°N$ plotted against July mean TOA outgoing longwave irradiance: (a) results from NOGAPS 3.3 (plus signs) and from ERB measurements (circles) and (b) results from NOGAPS 3.3MO (plus signs) and from ERB measurements (circles).

in several regions for both model versions. The models err on the low side over the Indian Ocean, for example, by as much as 72 W m^{-2} for the NOGAPS 3.3 simulations and 74 W m^{-2} for the NOGAPS 3.3MO simulations. For several regions, including the Indian Ocean and the central Pacific Ocean, a comparison with Figure 3 shows that such low values of predicted outgoing longwave irradiance coincide with large amounts of simulated convective rainfall. That this correspondence is not universal is seen in the results obtained for Australia, Indonesia, and the tropical eastern Pacific Ocean. Off the west coasts of North America and the northern portion of South America, the model predicts too much outgoing longwave radiation. This observation is consistent with the general failure of the model to predict realistic amounts of low-level marine stratiform clouds.

4.3. Relationship Between Solar and Longwave Radiation Fields

To accurately simulate the net radiative forcing by clouds, it is reasonable to assume that a model must provide accurate forecasts of the correlation between longwave and solar radiation fields. In order to assess the effects of the model change studied here in this respect, scatterplots of TOA net solar irradiance versus TOA outgoing longwave

irradiance for NOGAPS 3.3 and NOGAPS 3.3MO are presented in Figure 8 along with the corresponding ERB data. The data shown are for $9° \times 9°$ regions that extend from the equator to $9°N$. We see a considerable improvement in going from the cloud grid cell averaging scheme of NOGAPS 3.3 to the maximal overlap scheme of NOGAPS 3.3MO. The apparent limitation of the cloud parameterization is manifested in both plots, however, in some very low values of outgoing longwave irradiance, the occurrence of which has already been noted in Figure 7. The results shown here support the conclusion that the substantial improvement in the solar irradiance field over convective regions obtained with the maximal overlap scheme (as seen in Figures 2 and 5) does not result primarily from a compensation by that scheme for errors in the parameterized cloud fields. Corresponding plots for midlatitudes to high latitudes show considerably less difference between the two model versions, a reflection of the fact that the models differ the most in the regions of greatest convective activity.

5. Response of Model Radiation Fields

5.1. Direct Effect on the Absorption of Solar Radiation

The comparisons presented in section 4 show that the change in cloud solar forcing examined here has a considerable effect on NOGAPS TOA and surface radiation fields. The observed changes may be attributable not only to the direct effect of the change in the treatment of cloud solar forcing but also to the response of the model cloud fields (and to a lesser extent the moisture field) to this change. In order to better understand the significance of the observed model response, we first address the question of the extent of the direct effect represented by the model change. An estimate of the magnitude of this effect was obtained by repeating the NOGAPS 3.3 simulations for the five Julys using the same cloud grid cell averaging scheme that was used for the original simulations and outputting diagnostic solar radiation fields calculated using the maximal overlap scheme.

The model response in the present simulations derives from the effect of the model change on the amount of solar radiation absorbed by the atmosphere and, for land regions, by the surface. (Because sea surface temperatures are set to observed values, the large change in surface solar irradiance over the oceans seen in the difference plots in Figure 5 has no effect on the simulations.) The relative contribution of each of these effects is illustrated in Figure 9, which shows the difference with respect to solar radiation absorbed by the surface (Figure 9a) and by the atmosphere (Figure 9b) between values obtained from solar irradiance fields diagnosed from the NOGAPS 3.3 July simulations using the maximal overlap scheme and fields based on the cloud grid cell averaging scheme for the same simulations. The amount of solar radiation found to be absorbed by the surface using the maximal overlap scheme is generally considerably greater than that obtained using the grid cell averaging scheme. This is true particularly over tropical convective regions, as is similarly observed in Figure 5. The amount of solar radiation found to be absorbed by the atmosphere using the two treatments of cloud solar forcing differs by rather modest amounts, with the grid cell averaging scheme yielding more absorption than the maximal overlap scheme. The observed difference nonetheless exceeds 10 W m^{-2} over

a) Surface
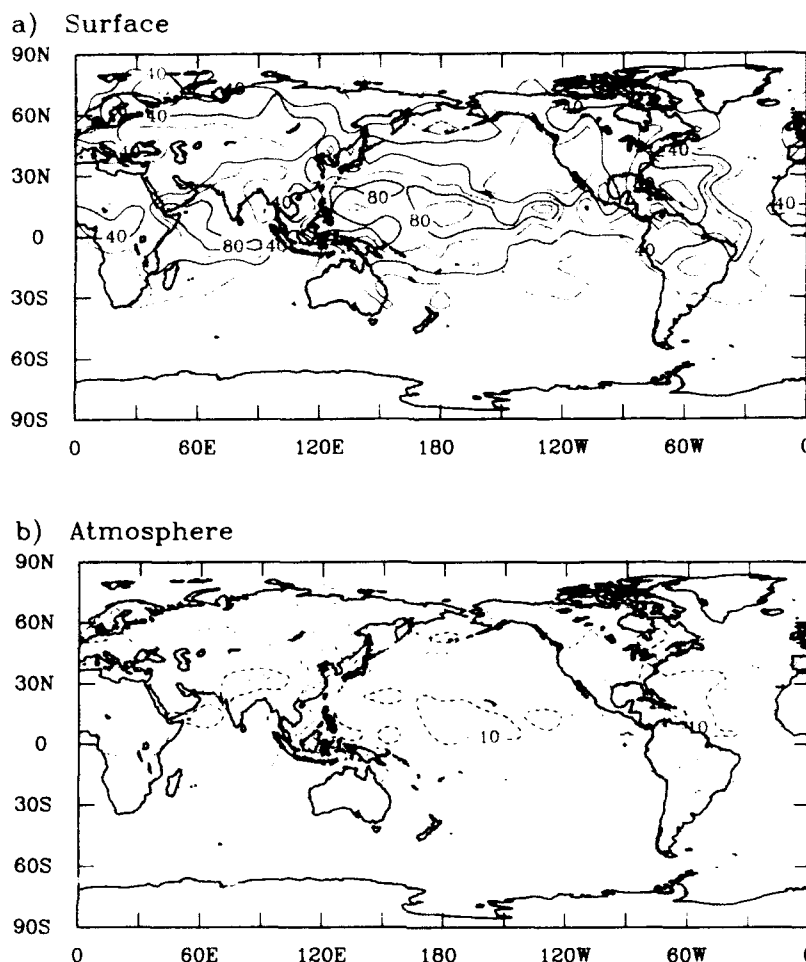
b) Atmosphere

Figure 9. Difference (in watts per square meter) with respect to the mean amount of solar radiation absorbed (a) at the surface and (b) in the atmosphere between values obtained using the maximal overlap scheme and values obtained using the grid cell averaging scheme for the NOGAPS 3.3 July simulations. The contour interval in Figure 9a is 20 W m^{-2} and that in Figure 9b is 5 W m^{-2}. The zero contour has been omitted. Negative contours are indicated by dashed lines. Shading is defined as in Figure 2.

extensive regions, particularly the tropical Pacific Ocean and the tropical and northern hemisphere subtropical Atlantic Ocean.

5.2. Response of Radiation Fields

One view of the model's response to the change in solar radiation treatments is seen in Figure 10. Figure 10a shows the difference between the diagnostic values from the NOGAPS 3.3 simulations of mean TOA net solar irradiance based on the maximal overlap treatment and the values calculated in the same simulations using the cloud grid cell averaging scheme. This plot represents the perturbation to the total absorption (surface and atmospheric) of solar radiation that results from the model change. In some regions the perturbation is considerable, the peak difference plotted here being 104 W m^{-2}. For comparison, the difference between the TOA solar irradiance field obtained with NOGAPS 3.3MO and the corresponding field obtained with the cloud grid cell averaging scheme in the NOGAPS 3.3 simulations is shown in Figure 10b. The plots exhibit many similarities, both showing considerably greater net solar irradiance from the maximal overlap scheme for the regions where the simulated convective rainfall rates are greatest

(see Figure 3). There are also some significant differences between the plots, reflecting the effect of the model response to the change in the treatment of cloud solar forcing. The response over continental convective regions is most notable, showing a negative feedback to the perturbation in solar irradiance seen in Figure 10a. This feedback results for the most part from the increase in the amount of convection over land in the NOGAPS 3.3MO simulations (see Figure 3b) that is generated by an increase in the flux of solar radiation at the surface. Such a feedback was similarly suggested in a GCM experiment carried out by *Randall et al.* [1989], in which the effects of cumulonimbus anvils were investigated.

The model response is more directly seen in Figures 11a and 11b. In Figure 11a the difference is plotted between the values of TOA net solar irradiance predicted in the simulations with NOGAPS 3.3MO and the corresponding results diagnosed from the NOGAPS 3.3 simulations using the maximal overlap scheme. Figure 11b shows the difference in mean TOA outgoing longwave irradiance between the two sets of simulations. In Figure 11a the model response is dominated by an effective decrease in the amount of net solar irradiance over continental regions. This decrease

a) NOGAPS 3.3 (maximal overlap – grid–cell–averaging)

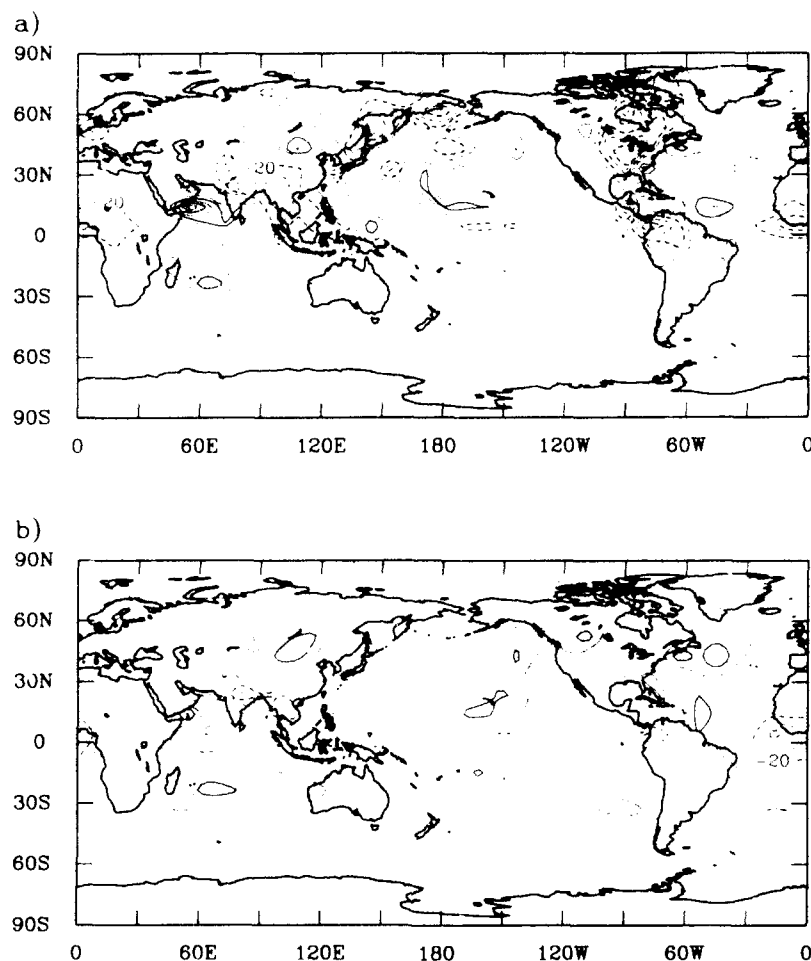b) NOGAPS 3.3MO – NOGAPS 3.3 (grid–cell–averaging)
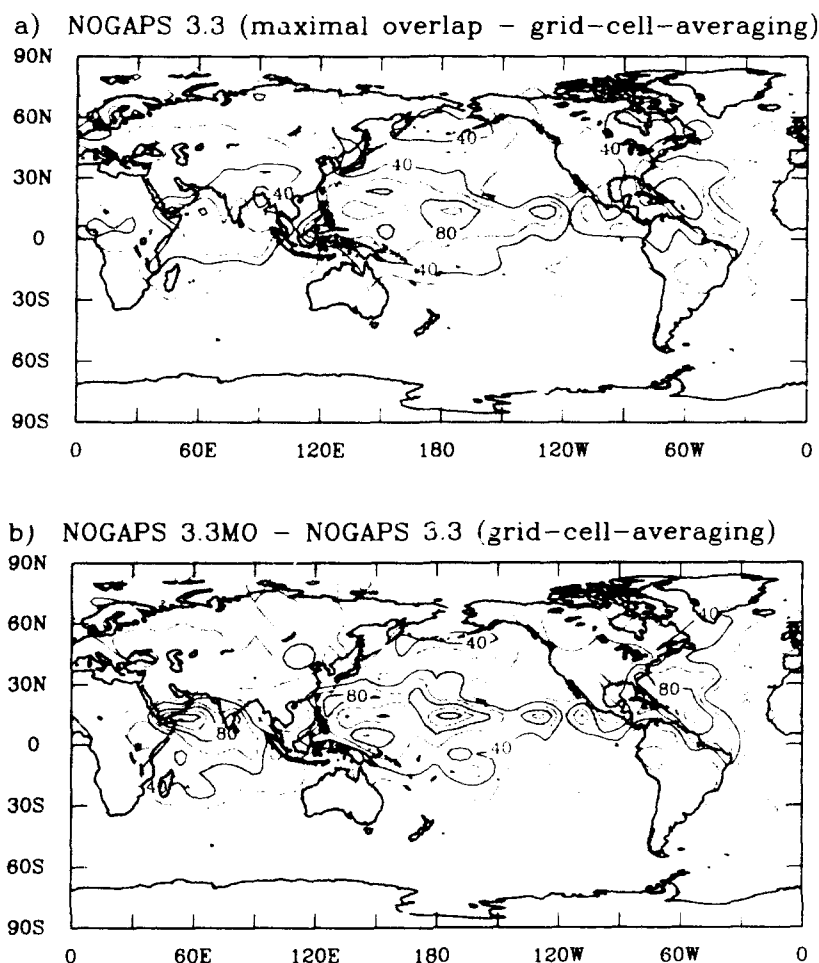
Figure 10. (a) Difference (in watts per square meter) between July mean TOA net solar irradiance diagnosed from the NOGAPS 3.3 simulations using the maximal overlap solar radiation scheme and the values obtained using the grid cell averaging scheme from the same simulations and (b) difference (in watts per square meter) between July mean TOA net solar irradiance from NOGAPS 3.3MO and the corresponding results obtained using the grid cell averaging treatment in the NOGAPS 3.3 simulations. Shading and contours are defined as in Figure 2.

reflects the negative feedback discussed in the preceding paragraph, through which the reduction in albedo that results from the change in the treatment of cloud solar forcing tends to generate an increased amount of convection over landmasses. The peak differences observed here, in the range of 30–50 W m⁻² in some areas, are fairly large.

Whereas the solar irradiance differences in Figure 11a are more pronounced over continental regions, the corresponding differences in outgoing longwave radiation seen in Figure 11b are more balanced in their distribution over land and water. There is a moderate decrease in outgoing longwave irradiance off the west coast of Africa for the simulations with NOGAPS 3.3MO and also over a portion of India, corresponding to similar solar irradiance differences shown in Figure 11a. These results suggest an increase in the amount of cloudiness predicted for these regions with the revised model. Increases in outgoing longwave irradiance are also observed, especially over the oceans, central Asia, and the northwest coast of North America. Whereas for Central America, much of eastern North America, and parts of the Pacific coast of Asia Figure 11a shows some fairly large differences in net solar irradiance associated with the

response to the model change, the differences in TOA outgoing longwave irradiance for these regions are rather small.

The latitudinal distribution of the perturbation in TOA downwelling solar irradiance (Figure 10a) that results from the change in the treatment of cloud solar forcing, and that of the model response in terms of TOA downwelling solar (Figure 11a) and longwave (Figure 11b, with a change in sign) irradiance, are plotted in Figure 12. Results are shown separately for land and ice (Figure 12a) and water (Figure 12b). Although the largest perturbations occur over water, the percentage response is generally greatest over land. In the tropics over land, there is a substantial negative response in TOA downwelling solar irradiance, tending to counter the perturbation, and a positive response in TOA downwelling longwave irradiance. Over land in the northern hemisphere midlatitudes the response in terms of downwelling solar irradiance is considerably less, not only in an absolute sense but also in relation to the perturbation. The corresponding response in downwelling longwave irradiance at midlatitudes is negative, in contrast to the situation in the tropics. The net response in TOA downwelling irradiance in both the tropics

a)

b)

Figure 11. (a) Difference (in watts per square meter) between July mean TOA net solar irradiances from the NOGAPS 3.3MO simulations and the corresponding results from the NOGAPS 3.3 simulations diagnosed using the maximal overlap solar radiation scheme and (b) difference (in watts per square meter) between July mean TOA outgoing longwave irradiances obtained in the simulations with NOGAPS 3.3MO and NOGAPS 3.3. The contour interval in both figures is 10 W m^{-2}, and the zero contour has been omitted. Negative contours are indicated by dashed lines. Shading is defined as in Figure 2.

and midlatitudes is negative. Despite the significantly greater response in TOA downwelling solar irradiance over land in the tropics, the net response in TOA downwelling irradiance as a percentage of the mean perturbation tends to be greater in magnitude at midlatitudes, as seen in Table 1.

6. Response of Model Cloud Fields

The radiation differences seen in Figure 11 result largely from changes in the predicted cloud fields. These changes may include changes both in cloud fraction and in cloud optical thickness at different model grid levels. The change in total cloudiness that results from the change in the treatment of cloud solar forcing is shown in Figure 13. The increases in cloudiness off the west coast of Africa and over a portion of India that are suggested by the change in outgoing longwave radiation in Figure 11b are both evident in this plot. In general, the changes in total cloudiness tend to be better correlated with changes in longwave rather than solar irradiance. Although the changes in cloudiness observed over land are generally associated with changes in convective activity, the changes over the oceans tend to

occur away from convective regions (see Figure 3) and generally reflect a decrease in moisture at mid to upper levels. The significant decreases in cloudiness at midlatitudes are responsible for the negative response of the model there in terms of TOA longwave irradiance noted in section 5.2.

Although cloud optical thickness data were not saved from the model runs, estimates of cloud optical thickness were made on the basis of model July mean temperature fields for cloud layers 500 m thick. The fractional changes in optical thickness obtained for the two model versions at 850 mbar, 500 mbar, and 200 mbar are plotted in Figure 14. We find that cloud optical thicknesses are generally greater for NOGAPS 3.3MO, reflecting a warming of the troposphere that will be discussed in section 7.3. Note that only results obtained for stable clouds are shown here. Results obtained for convective clouds are generally similar, except where temperatures are substantially below freezing. Where clouds composed of both liquid water and ice exist, the fractional changes obtained for convective clouds are generally considerably smaller than those for stable clouds because of the greater

a)

b)
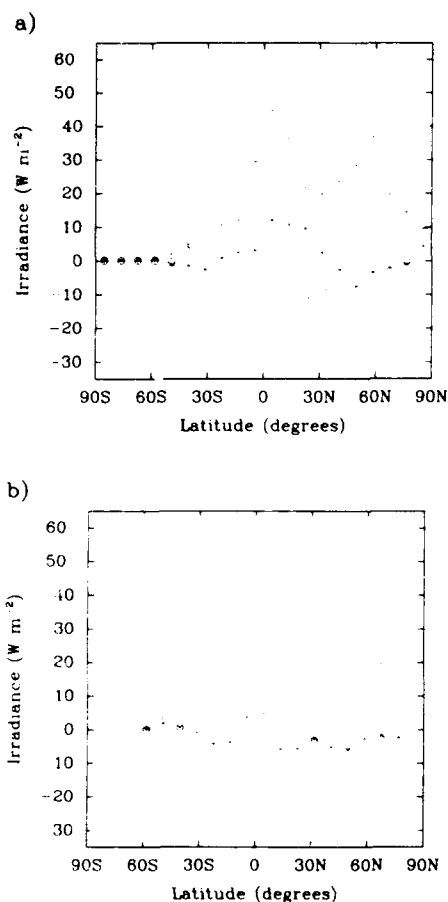
Figure 12. Zonal perturbation in TOA downwelling solar irradiance represented by the change in the treatment of cloud solar forcing (plus signs) and changes in TOA downwelling solar (circles) and longwave (asterisks) irradiance that result from the model response to that perturbation. Results are shown for (a) land and ice and (b) water.

ice contents assumed for convective clouds. At lower levels the increases in optical thickness occur largely over continental regions, though generally not over the most convectively active areas, as seen by comparison with Figure 3. The increases in cloud optical thickness tend to counter the increased surface absorption of solar radiation that results from the change in the treatment of cloud solar forcing.

Table 1. Changes in TOA Downwelling Irradiance Over Northern Hemisphere Land

| Latitudinal Zone	Perturbation, W m⁻²	Response		
		Solar, W m⁻²	Longwave, W m⁻²	Total, %
0°–9°N	45.5	23.7	10.1	(−)30.0
9°–18°N	38.7	14.9	8.0	(−)18.0
18°–27°N	22.7	10.8	8.2	(−)11.5
27°–36°N	18.3	8.5	1.7	(−)37.5
36°–45°N	20.0	5.7	3.1	(−)43.8
45°–54°N	28.3	5.8	7.4	(−)46.7
54°–63°N	32.2	8.4	4.0	(−)38.7
63°–72°N	19.7	3.3	2.4	(−)29.1
72°–81°N	15.3	1.0	1.5	(−)16.5
81°–90°N	9.6	1.7	4.0	23.7

though their actual effect on the solar radiation field will depend on the vertical profile of cloudiness in a given region.

The effects of changes in cloudiness on the radiation fields are most clearly seen in the corresponding changes in cloud radiative forcing. Plots showing the changes in surface cloud solar forcing and atmospheric cloud longwave forcing that result from incorporating the maximal overlap scheme into the model are shown in Figures 15a and 15b, respectively. The cloud solar forcing changes shown in Figure 15a were calculated using the maximal overlap treatment for both sets of simulations. Negative values in Figure 15a reflect increased cloud solar forcing, and positive values in Figure 15b reflect increased cloud longwave forcing. We do not show the changes in cloud solar forcing of the atmosphere or cloud longwave forcing of the surface, because these changes are considerably smaller than those plotted here, as one may expect on the basis of the modeling study of *Slingo and Slingo* [1988]. To a considerable degree, changes in surface cloud solar forcing are correlated with perturbations in surface solar absorption shown in Figure 9a. Although the largest such perturbations occur in the tropics, they occur most extensively there over the oceans where there is no surface response in the present model; hence the observed cloud feedback over land is more evenly distributed latitudinally than might otherwise be expected. The relative response of the model in terms of the ratio of the change in cloud surface forcing to the perturbation shown in Figure 9a is in many regions very large, showing the importance of improvements in the treatment of cloud solar forcing for cloud field prediction. Over the oceans the effect of cloud feedback on absorption of longwave radiation by the atmosphere tends to reinforce the direct cooling effect of the change in the treatment of cloud solar forcing seen in Figure 9b. These effects are not strongly correlated spatially, however, there being a greater effect of cloud feedback at higher latitudes than might be expected from the direct perturbation in atmospheric absorption. Over land, because of the increased convective activity that results from the surface response, changes in atmospheric absorption of longwave radiation tend to counter the direct cooling effect seen in Figure 9b. The latitudinal dependencies of the changes in cloud solar forcing of the surface and longwave forcing of the atmosphere are shown in Figure 16 for land and ice (Figure 16a) and water (Figure 16b). A comparison with Figure 12 shows that most of the change in TOA downwelling solar irradiance shown there is accounted for by the changes in surface absorption shown in Figure 16. To some extent, changes in TOA downwelling longwave irradiance and changes in atmospheric absorption are similarly related, but in this case, changes in temperature and moisture also play a significant role.

7. Response of Model Precipitation and Temperature Fields

7.1. Precipitation Response

The change in convective precipitation rate was shown in Figure 3b. Although most of the precipitation increases over land are from convective precipitation, there is a large increase (as much as 8 mm d⁻¹) in large-scale precipitation over land near the Bay of Bengal. The change in the difference between precipitation and evaporation is plotted
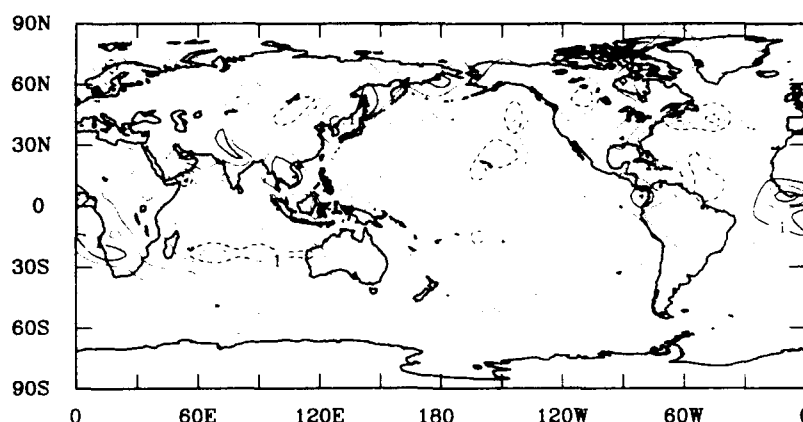
Figure 13. Change in July mean total cloudiness (assuming maximally overlapping clouds). The contour interval is 0.05. Shading is defined as in Figure 2.

in Figure 17, showing that there is a tendency toward an increase in this quantity over several continental regions, most notably near the Bay of Bengal and central Africa, reflecting an increased flux of moisture from sea to land. The relationship between convective rainfall rate and surface cloud solar forcing is also affected by the model change. This fact is illustrated in Figure 18, which shows for the two model versions the surface cloud solar forcing plotted against convective precipitation rate for $9° \times 9°$ continental regions extending from $0°$ to $9°N$. We find, as one expects, that convective rainfall tends to increase with increased surface cloud solar forcing and that for a given convective rainfall rate, the surface cloud solar forcing predicted by NOGAPS 3.3 generally exceeds that predicted by NOGAPS 3.3MO by 30–50 W m^{-2}. Somewhat greater changes in this relationship are observed over water. These changes are reflected over land in changes in the corresponding relationships for other surface fluxes.

7.2. Surface Response

As shown in Figure 19, there are some significant ground temperature changes associated with the change in the treatment of cloud solar forcing. Ground temperatures generally increase over continental regions, consistent with what one may expect on the basis of the increase in surface solar irradiance shown in Figure 9a. The relationship between the temperature increase and the perturbation in the absorption of solar radiation at the surface shown in Figure 9a, however, is found to vary considerably. Note, in particular, that the large increase in ground temperature over central Asia occurs where the perturbation in surface solar irradiance is less than 40 W m^{-2}, whereas larger perturbations over central Africa, India, and North and South America are accompanied by significantly smaller temperature increases. The observed response of the land surface must therefore reflect variations in the model response in terms of cloud feedback and latent and sensible heating. One finds, for example, by comparing these observations with Figure 15a, where the effect of cloud feedback on surface solar irradiance is shown, that the region over central Asia where there is a substantial increase in ground temperature is distinguished by the absence of the negative feedback observed over other regions. There appears to be some

tendency, in fact, for the model to produce a positive feedback in this region. Referring to Figure 3b, one sees that the general increase in convective precipitation over continental regions is not observed over much of central Asia, possibly the result of a change in the large-scale circulation.

Although the lack of a negative cloud feedback on surface solar irradiance over central Asia helps to explain the variability in the simulated changes in ground temperature to some extent, this facet of the simulations does not fully explain the simulated temperature change variations. This fact can be seen by comparing the ground temperature differences in Figure 19 with Figure 20, which shows the net change in surface solar irradiance, including the effect of the model response. The net change in surface solar irradiance is to a considerable degree a worse indicator of ground temperature changes than the perturbation in surface solar irradiance plotted in Figure 9a. For example, although the net increase in surface solar irradiance over portions of India exceeds the corresponding increase over central Asia, the change in ground temperature over India is very small. On the other hand, the observed increase in ground temperature over central Africa is accompanied by only scattered modest increases in surface solar irradiance.

The lack of any significant increase in ground temperature over India is explained by Figure 21, which shows the change in surface latent heating (positive values indicating increased evaporation and surface cooling). There is a region of significantly enhanced evaporation over India which overlaps, but is not coincident with, a region of enhanced convective precipitation seen in Figure 3b. This increase in surface evaporation largely offsets the increase in surface solar irradiance over India seen in Figure 20. The change in surface evaporation is almost everywhere considerably greater than either the change in surface sensible heating or the change in the net surface emission of longwave radiation. Exceptions occur, however, in arid regions such as central Asia, where increases in evaporation are necessarily limited. The increased evaporation appears to result, to a considerable extent, from increased surface wind velocities, though in regions of enhanced precipitation, increased low-level drying caused by the model's Arakawa-Schubert cumulus parameterization and increased availability of surface mois-

a)

b)

c)
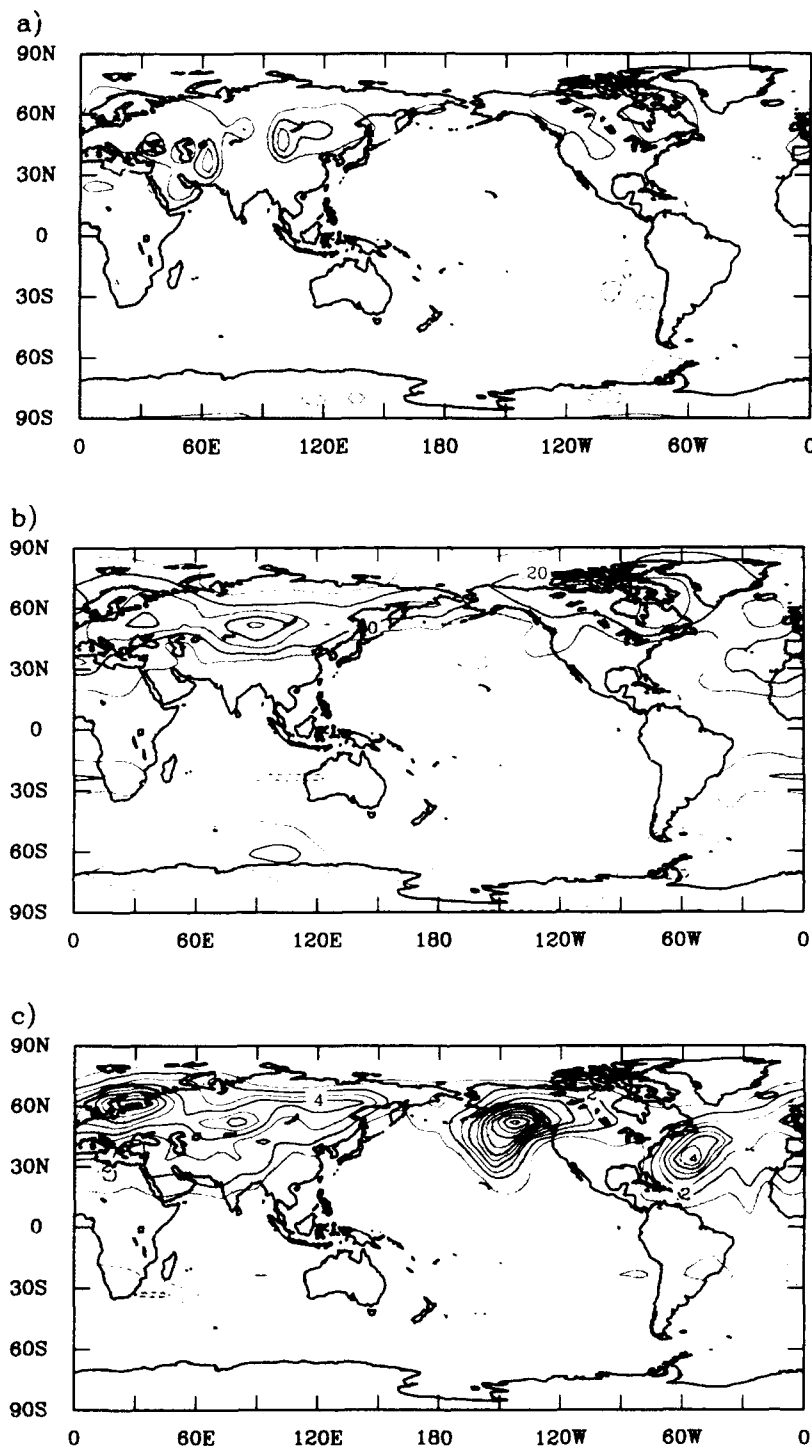
Figure 14. Fractional change in optical thickness of stable clouds calculated using July mean temperature fields. Results are shown for (a) 850 mbar, (b) 500 mbar, and (c) 200 mbar. The contour interval is 0.1. Shading is defined as in Figure 2.

ture for evaporation are also likely factors. Over the oceans, there appears to be a tendency for increased evaporation where there has been a reduction in low-level moisture. Comparing Figure 21 with Figure 22, which shows the change in 1000-mbar specific humidity, we see such a correlation, for example, to the east of Madagascar and off the west coast of South America.

7.3. Atmospheric Stability

The observed increases in convective activity reflect destabilization of the atmosphere near the surface brought about by the increased surface heating and the response of the model's revised Arakawa-Schubert convective parameterization. Changes in the temperature lapse rate of the

a)

b)
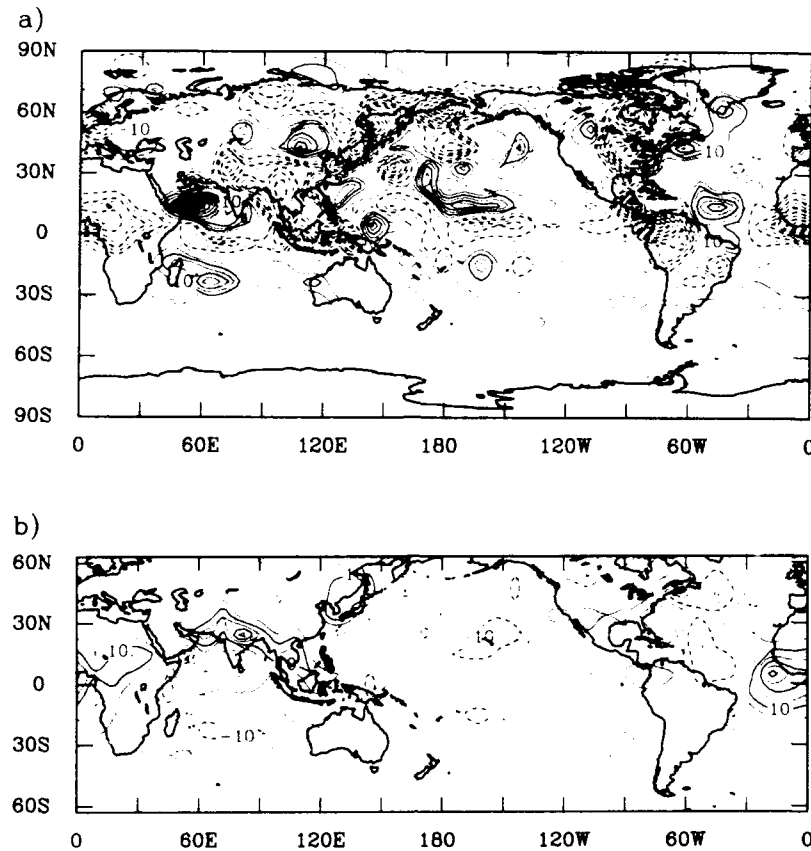
Figure 15. Change in July mean surface cloud (a) solar forcing and atmospheric cloud (b) longwave forcing. The results plotted in Figure 15a were obtained using the maximal overlap treatment for both sets of simulations. The contour interval in both plots is 5 W m^{-2}. Shading is defined as in Figure 2.

atmosphere over convective regions show to some extent the degree to which the convective parameterization counters the tendency toward decreased atmospheric stability, though changes in atmospheric moisture can significantly affect atmospheric stability as well. Concerning an experiment with the UCLA/GLA GCM, *Randall et al.* [1989] hypothesized that the cause of a substantial increase in temperature in the northern hemisphere midlatitudes that tended to stabilize the atmosphere was the response of the Arakawa-Schubert scheme in the model to destabilization brought about by increased atmospheric moisture. In the Randall et al. experiment the GCM was run for July conditions, and the effect of convective anvils was tested by removing them. The model change studied in the present work has a similar, though not as dramatic, effect on solar radiation fields as removing convective anvils. There are some significant differences between these studies as well, however, including the fact that in the present work there is no direct effect on longwave radiation, and cloud feedback is allowed. In order to investigate any changes in atmospheric conditional instability associated with changes in temperature in the present simulations, we show in Figure 23 the change in temperature lapse rate between the 850-mbar and the 500-mbar levels. We see some evidence of stabilization (decreased lapse rate) at mid to high latitudes in the northern hemisphere, though there are regions of destabilization in these latitudinal zones as well, particularly over Asia and central North America. Comparing this plot with the plot of

changes in the convective precipitation rate shown in Figure 3b, we note that the increase in convective precipitation over Colombia seen in Figure 3b corresponds to a small increase in temperature lapse rate, whereas increased convective precipitation over western Africa occurs where there is a small decrease in temperature lapse rate. Differences in atmospheric moisture may explain this difference, but this point is not clear. A look at Figure 24, which shows the change in precipitable water amount, reveals a significant increase over western Africa, consistent with the theory that destabilization by increased low-level moisture in convective regions results in a decrease in temperature lapse rate. Over Colombia there is a large region with no significant change in precipitable water (suggesting that the increases in temperature lapse rate in that region is not inconsistent with this theory), but a regional increase in precipitable water is also observed there. It should be noted that some of the largest changes in lapse rate in Figure 23 actually occur away from convectively active regions, supporting the argument against the model's convective scheme's being the primary cause of such changes.

The extent of atmospheric temperature changes is more clearly seen in Figure 25, which shows the temperature changes at 850 mbar (Figure 25a), 500 mbar (Figure 25b), and 200 mbar (Figure 25c). The large increase in temperature at midlatitudes in the northern hemisphere bears some resemblance to the zonal temperature increase noted by *Randall et*

a)

b)
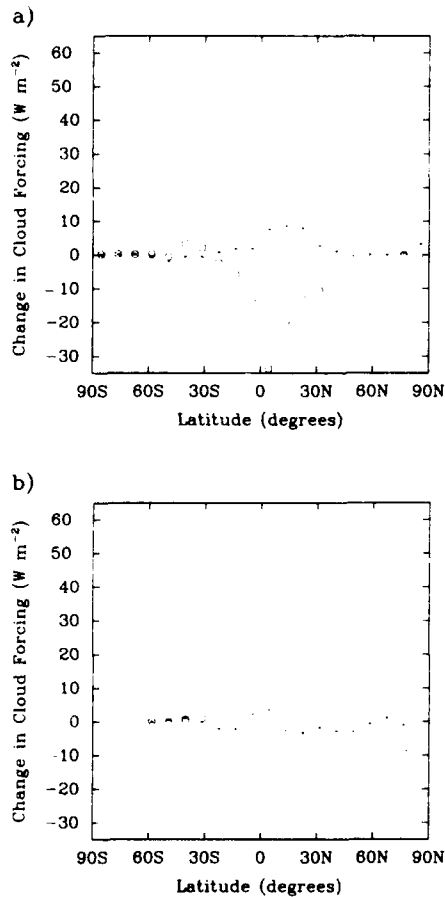
Figure 16. Zonal changes in surface absorption of solar radiation (circles) and atmospheric absorption of longwave radiation (asterisks) that result from the model response to the change in the treatment of cloud solar forcing. Results are shown for (a) land and ice and (b) water.

al. [1989]. The temperature increase at 850 mbar observed here is greatest over arid central Asia, where the large ground temperature increase noted in the preceding section is observed (Figure 19). There is also a large region of increased temperature over northern North America. At 500 mbar the region of increased temperature is considerably
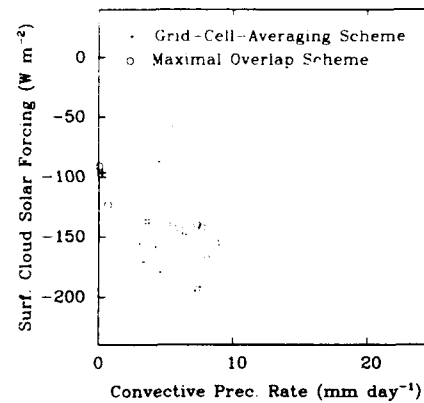

Figure 18. July mean surface cloud solar forcing as a function of convective precipitation rate for 9° × 9° continental regions extending from 0° to 9°N. Results are shown for NOGAPS 3.3 (plus signs) and NOGAPS 3.3MO (circles).

more extensive but largely confined to mid and high latitudes. At 200 mbar the greatest temperature increases are found over the Atlantic and northern Pacific Oceans. Noting the strong correlation between increases in 850-mbar temperature and increases in ground temperature, it appears that the low-level temperature increases in the present simulations result from increases in surface sensible heating and emission of longwave radiation and from increases in vertical eddy or shallow convective transport. The temperature increases at mid to upper levels may, to some extent, reflect the vertical eddy transport and advection of air heated at lower levels. Changes in radiative heating may possibly be a factor in the temperature changes as well. Although the direct effect of the model change on atmospheric heating, shown in Figure 9b, is to cool the atmosphere, Figure 15b shows that the cloud response to the model change tends to warm the atmosphere over certain regions, including southern Asia and western Africa.

8. Discussion and Conclusions

The NOGAPS forecast model results and ERB satellite data presented in section 4 show a considerable improvement in solar radiation fields with the assumption of maxi-
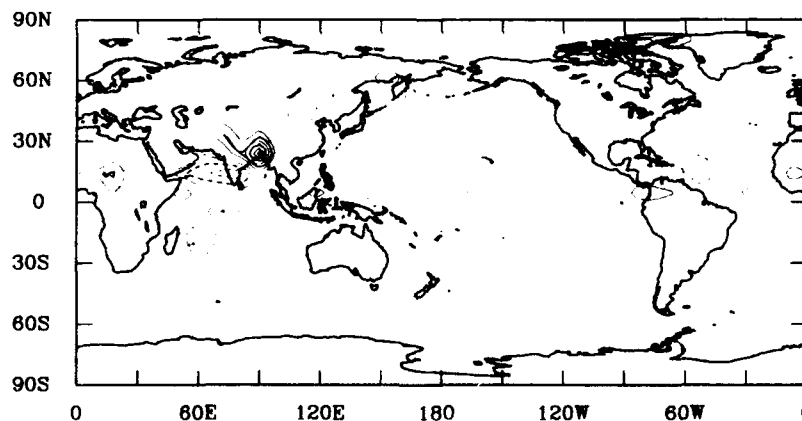

Figure 17. Change in July mean difference between the rate of precipitation and the rate of evaporation. The contour interval is 2 mm d⁻¹. Shading is defined as in Figure 2.
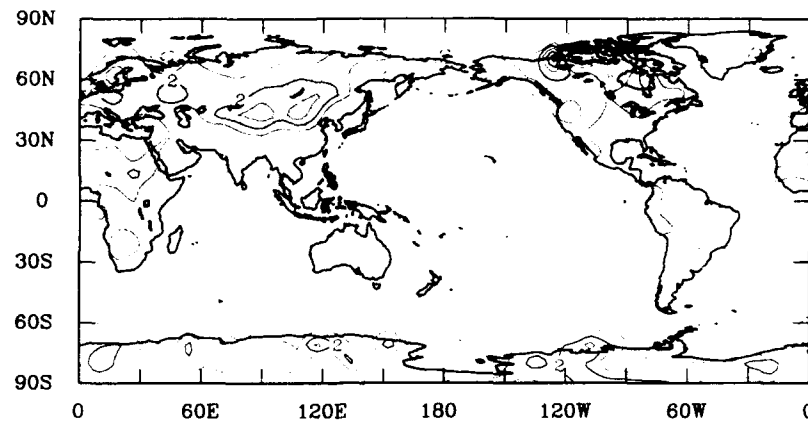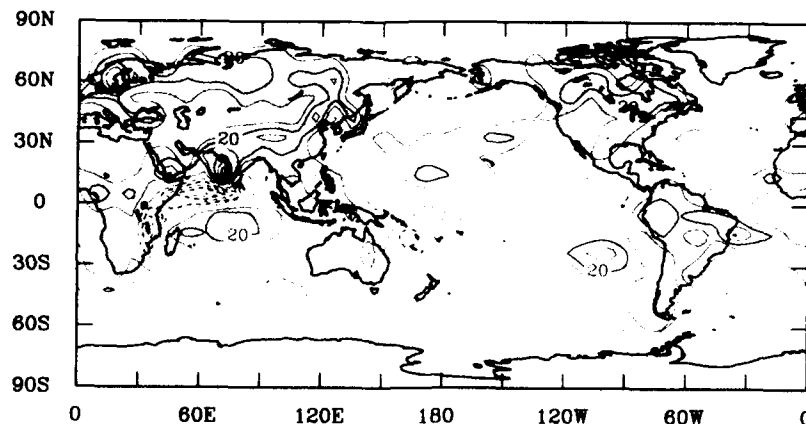
Figure 19. Change in July mean surface temperature (in degrees Kelvin). The contour interval is 1 K. Shading is defined as in Figure 2.

mally overlapping clouds in the treatment of cloud solar forcing. The improved correlation between the TOA solar and the longwave irradiances demonstrated in section 4.3 supports the conclusion that this improvement is not merely the result of a compensation for errors due to inadequacies in the model's cloud parameterization. The results obtained

should be expected, because the change in the solar radiation scheme addressed here brings consistency between the treatment of fractional cloudiness in the solar and longwave radiation schemes of the model. Because of the relatively low optical thickness of most nonconvective clouds parameterized in the GCM simulations studied here, the most
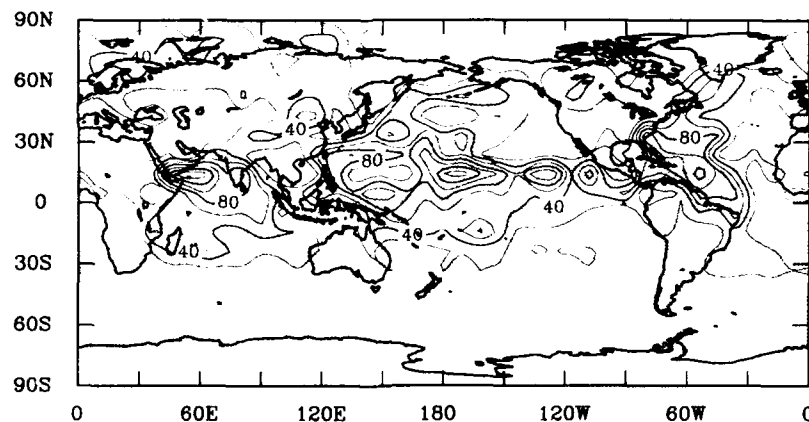
Figure 20. Change in July mean surface solar irradiance (in watts per square meter), reflecting both the change in cloud solar forcing treatment and the model response. The contour interval is 20 W m^{-2}. Shading is defined as in Figure 2.

Figure 21. Change in July mean surface latent heating (in watts per square meter). The contour interval is 10 W m^{-2}. Shading is defined as in Figure 2.
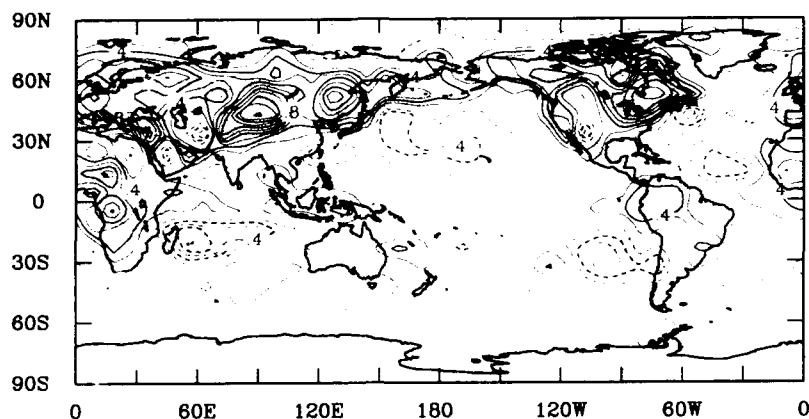
Figure 22. Change in July mean 1000-mbar specific humidity (in grams per kilogram). The contour interval is 0.2 g kg^{-1}. Shading is defined as in Figure 2.

significant improvement in model solar radiation fields was shown in section 4 to be in regions of deep convection. We found, for example, that improvements in simulated surface solar irradiances exceed 100 W m^{-2} in portions of the tropical Pacific Ocean.

The dominant model response in the present study is the observed increase in convective precipitation and cloudiness over continental regions that results from the increased amount of surface solar radiation. Along with the increase in continental convection, there is a tendency for an increased flux of moisture from sea to land. Substantial fractional increases in cloud water content are found to occur, for the most part associated with extensive regions of increased tropospheric temperature in the northern hemisphere midlatitudes.
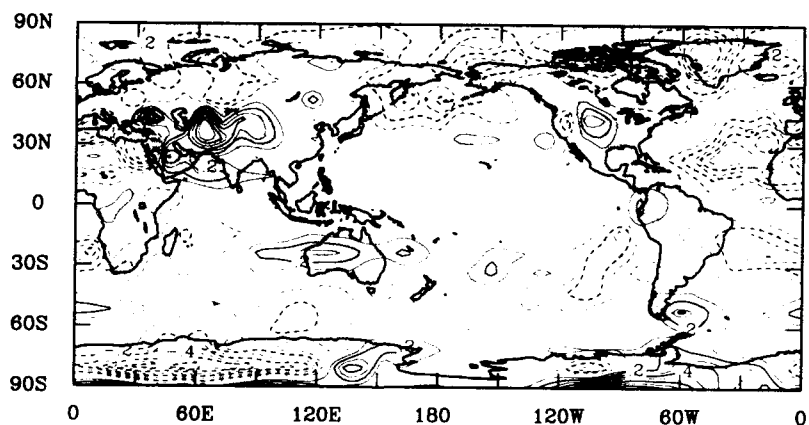
Figure 23. Change in July mean temperature lapse rate between 850-mbar and 500-mbar levels. The contour interval is 0.1 K km^{-1}. Shading is defined as in Figure 2.
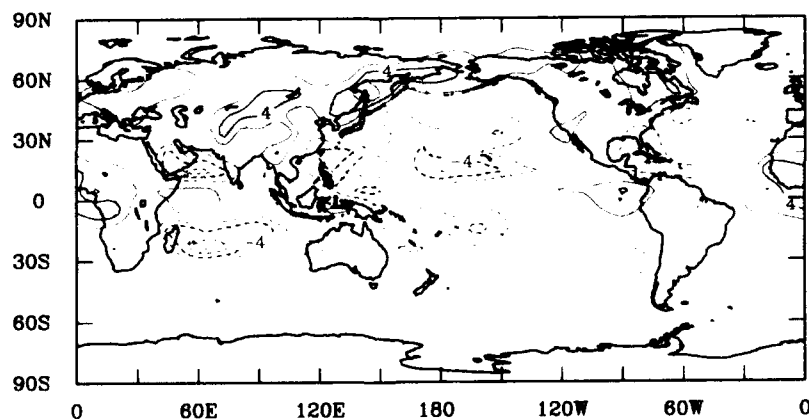
Figure 24. Change in July mean precipitable water amount (in millimeters). The contour interval is 2 mm. Shading is defined as in Figure 2.
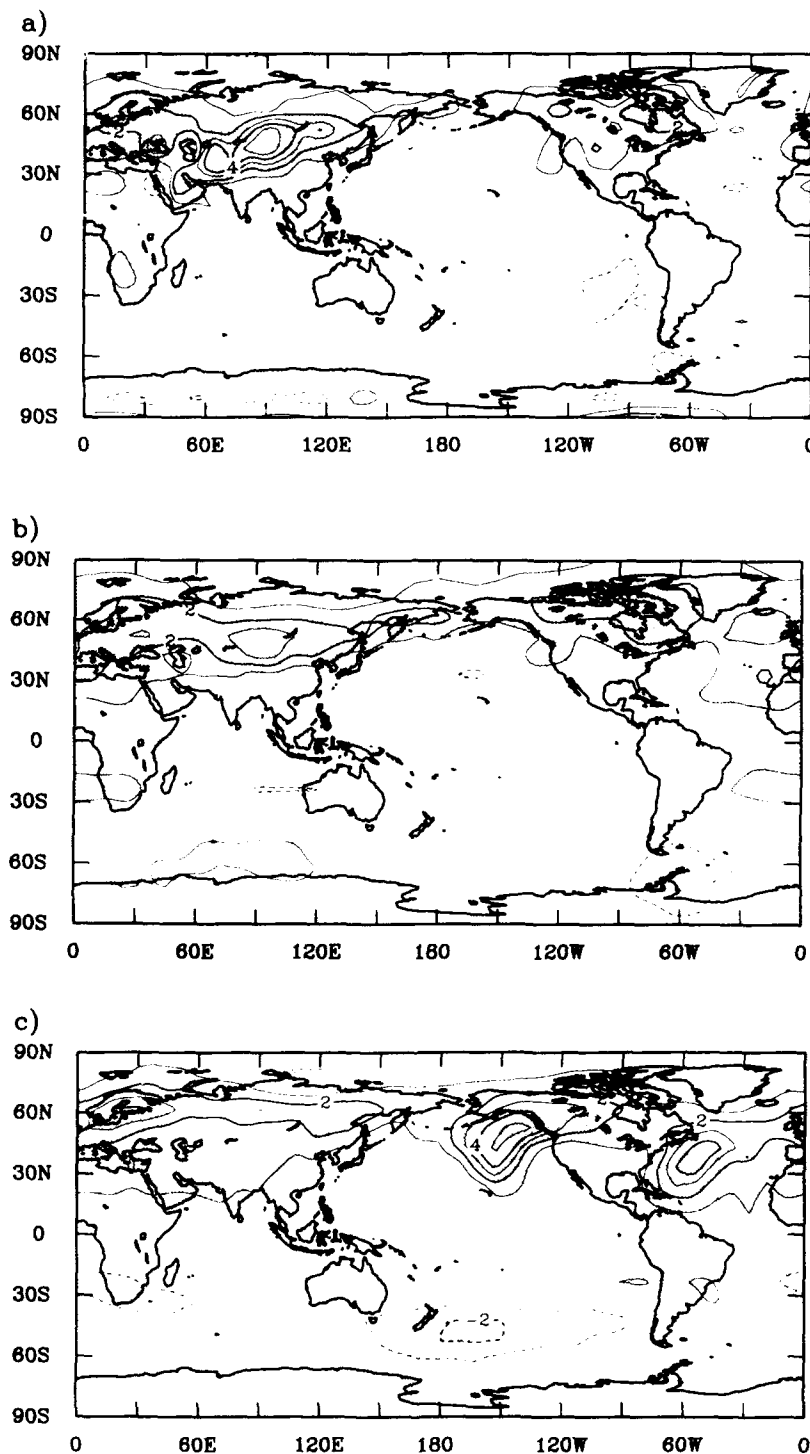
Figure 25.   Change in July mean temperature (in degrees Kelvin) at (a) 850 mbar, (b) 500 mbar, and (c) 200 mbar. The contour interval is 1 K. Shading is defined as in Figure 2.

Clouds generally act as a negative feedback to the perturbation in solar irradiance represented by the model change. Estimates of this perturbation were obtained as the difference between solar irradiances diagnosed (but not used in the model) assuming maximally overlapping clouds and solar irradiances produced (and used in the model) in the same simulations by the unrevised NOGAPS cloud solar forcing scheme using grid cell averaged clouds. With respect to the perturbation defined in this way, the model response in

terms of the change in surface cloud solar forcing computed for maximally overlapping clouds is in some regions quite large. This large response is responsible for the relatively small reduction observed in the error in TOA downwelling solar irradiance over land in certain regions, notably India and portions of Africa and eastern North America, and shows the importance of improvements in the treatment of cloud solar forcing for cloud field prediction.

Over land in the northern hemisphere the model response

in terms of the change in TOA downwelling solar irradiance evaluated using the maximal overlap treatment is appreciably greater in the tropics than at midlatitudes. For example, between the equator and 9°N the mean response is −23.7 W m⁻², or 52% of the 45.4 W m⁻² perturbation in TOA downwelling solar irradiance represented by the model change. The corresponding response between 45°N and 54°N is −5.8 W m⁻², or 21% of the 28.3 W m⁻² perturbation at that latitudinal zone. We find, however, that because of latitudinal differences in the response of the model's longwave radiation field the percentage net response in TOA downwelling irradiance at midlatitudes tends to exceed that in the tropics.

Changes in ground temperature observed here reflect a number of factors, including cloud cover, surface moisture, and large-scale dynamics. The tendency for ground temperature to increase in convective regions because of increased surface solar irradiance is moderated to a considerable degree by cloud feedback and increased surface evaporation. Increases in surface sensible heating and net emission of longwave radiation are limited largely to regions where these other factors do not act to limit temperature increases. Central Asia is the most notable example of such regions, observed in the present study. It experiences a decrease in precipitation and cloud cover. Evaporation does not increase enough to be a significant factor in limiting the resulting ground temperature increase because of the small amount of ground moisture. The extensive atmospheric temperature increases in the northern hemisphere midlatitudes appear to be associated, at least at low levels, with such ground temperature increases.

Although improved agreement of NOGAPS solar radiation fields with ERB data has been demonstrated with the maximal overlap treatment of cloud solar forcing, considerable errors remain. As indicated in section 1, these errors may derive from a number of sources. We have shown in the present study that the model's solar radiation field is very sensitive to the treatment of fractional cloudiness, and further work is needed to determine the extent of the remaining errors associated with this treatment. On the basis of their study of cloud overlap statistics over the North Atlantic during January 1979, Tian and Curry [1989] noted that although the maximal overlap assumption appears to be a good approximation for adjacent cloudy layers, the random overlap assumption is a better approximation for cloudy layers separated by clear interstices. The solar radiation scheme of Geleyn and Hollingsworth [1979] is somewhat consistent with these observations [cf. Ritter and Geleyn, 1992], though its application of the maximal overlap assumption for adjacent cloudy layers assumes no horizontal variation of solar irradiance within the cloudy or clear portions of a given model grid cell. Composite schemes of this type may prove to be acceptable solutions for the radiation treatment of fractional cloudiness in global models, but a compelling empirical basis for any such solution must await further studies of the regional and seasonal dependencies of the structure of cloud fields.

Appendix: Parameterization of Cloud Optical Thickness in NOGAPS

Cloud optical thicknesses produced by NOGAPS 3.3 are based on separate calculations for stable and convective

clouds. In general, the optical thickness is taken to be a weighted sum of values calculated for water and ice clouds. The weighting varies linearly with temperature within the temperature range 233.16–273.16 K and produces optical thicknesses consistent with all ice clouds at temperatures of 233.16 K and less and all water clouds at temperatures of 273.16 K and greater.

For water clouds the optical thickness τ_l of a cloud layer corresponding to a model grid level of thickness Δz is taken to be proportional to the liquid water path following Stephens [1978a], with liquid water content w_l assumed to be proportional to the saturation specific humidity q_s. Thus

$$\tau_l = 3LWP/2r_e, \tag{1}$$

where

$$LWP = w_l \Delta z \tag{2}$$

and

$$w_l = cq_s. \tag{3}$$

Appropriate values for the equivalent radius r_e of the drop size distribution and for the parameter c vary widely, depending on cloud type. In the current NOGAPS parameterization a value of 0.0079 is used for c for stable clouds, which yields a liquid water content of 0.14 g m⁻³ at 20°C. This liquid water content corresponds to one of the stratocumulus drop size distributions in Table 4 of Slingo and Schrecker [1982]. The equivalent radius given for that drop size distribution is 5.4 μm, which is the value used in NOGAPS for r_e in the case of stable clouds. For convective water clouds the value used for c is 0.013, which gives a liquid water content of 0.23 g m⁻³ at 20°C. The equivalent radius for this case was taken to be 5.5 μm, the same as that used by Stephens [1978b] for fair weather cumulus. The liquid water content cited here is less than the value used by Stephens (1.0 g m⁻³) and appears to be too low, except for very small clouds. Warner [1955, 1969] frequently observed peak water contents in cumulus clouds in the range of 0.5–1.5 g m⁻³, though values on the order of 25% less than the peak values may be justified for use in a cloud parameterization on the basis of the substantial variability he observed within clouds. Warner [1955] generally found the water content to peak near cloud top, a feature which is not reproduced in the present formulation of the scheme because of the unrealistic decline in liquid water content with height given by (3).

For ice clouds the optical thickness τ_i of a given cloud layer corresponding to a model grid level of thickness Δz is obtained from its definition,

$$\tau_i = w_i k_i \Delta z, \tag{4}$$

where w_i is the ice water content and k_i is the extinction coefficient. The extinction coefficient is given by

$$k_i = \sigma_e / V_i \rho_i. \tag{5}$$

where σ_e is the extinction cross section, V_i is the volume of a typical ice crystal, and ρ_i is the density of ice. The value used for V_i corresponds to columnar ice crystals of radius 60 μm and length 300 μm. This crystal size falls within the range observed in several observational studies [Liou, 1986]. The corresponding extinction cross section, 5.653 × 10⁻⁸

m^2, given by *Liou* [1986] and based on a numerical calculation, is used for σ_e. Values used for the ice water content differ for stable clouds and convective clouds. For stable clouds, w_i is given in units of grams per cubic meter by

$$w_i = 0.028 \qquad\qquad |T| \le 20°C$$

$$\ln (w_i) = -7.6 + 4 \exp [-0.2443 \times 10^{-3}(|T| - 20.)^{2.5}] \qquad (6)$$

$$|T| > 20°C$$

where T is the temperature in degrees Celsius. The expression used for $|T|$ greater than 20°C approximates the expression given by *Liou* [1986], which is based on data presented by *Heymsfield and Platt* [1984]. For $|T|$ less than 20°C the constant value assumed for w_i gives an approximately continuous temperature dependence of w_i. For convective clouds, w_i is assigned a constant value of 0.1 g m^{-3}, which may be somewhat low, on the basis of the range of from 0.15 to 0.25 g m^{-3} observed by *Heymsfield and Knollenberg* [1972] in cirrus-generating cells.

References

Ackerman, S. A., and G. L. Stephens, The absorption of shortwave solar radiation by cloud droplets: An application of anomalous diffraction theory, *J. Atmos. Sci.*, 44, 1574–1588, 1987.

Aida, M., Scattering of solar radiation as a function of cloud dimensions and orientation, *J. Quant. Spectrosc. Radiat. Transfer*, 17, 303–310, 1976.

Ardanuy, P. E., L. L. Stowe, A. Gruber, and M. Weiss, Shortwave, longwave, and net cloud-radiative forcing as determined from Nimbus 7 observations, *J. Geophys. Res.*, 96, 18,537–18,549, 1991.

Arking, A., and J. D. Childs, Retrieval of cloud cover parameters from multispectral satellite images, *J. Clim. Appl. Meteorol.*, 24, 322–333, 1985.

Bony, S., H. Letreut, J. P. Duvel, and R. S. Kandel, Satellite validation of GCM-simulated annual cycle of the Earth radiation budget and cloud forcing, *J. Geophys. Res.*, 97, 18,061–18,081, 1992.

Budyko, M. I., The effect of solar radiation variations on the climate of the earth, *Tellus*, 21, 611–619, 1969.

Buriez, J.-C., B. Bonnel, Y. Fouquart, J.-F. Geleyn, and J.-J. Morcrette, Comparison of model-generated and satellite-derived cloud cover and radiation budget, *J. Geophys. Res.*, 93, 3705–3719, 1988.

Cess, R. D., et al., Intercomparison and interpretation of climate feedback processes in 19 atmospheric general circulation models, *J. Geophys. Res.*, 95, 16,601–16,615, 1990.

Cess, R. D., Climate change: An appraisal of atmospheric feedback mechanisms employing zonal climatology, *J. Atmos. Sci.*, 33, 1831–1843, 1976.

Cess, R. D., and G. L. Potter, Exploratory studies of cloud radiative forcing with a general circulation model, *Tellus, Ser. A*, 39, 460–473, 1987.

Chandrasekhar, S., *Radiative Transfer*, 393 pp., Dover, Mineola, N. Y., 1960.

Chertock, B., Global monitoring of net solar irradiance at the ocean surface using Nimbus-7 satellite data, Doctoral dissertation, 118 pp., Scripps Inst. of Oceanogr., Univ. of Calif., San Diego, 1989.

Chertock, B., and Y. C. Sud, Comparison of ocean surface solar irradiance in the GLA general circulation model and satellite-based calculations, *J. Clim.*, 6, 560–567, 1993.

Chertock, B., R. Frouin, and C. Gautier, A technique for global

monitoring of net solar irradiance at the ocean surface, II, Validation, *J. Appl. Meteorol.*, 31, 1067–1083, 1992.

Davies, R., The effect of finite geometry on the three-dimensional transfer of solar irradiance in clouds, *J. Atmos. Sci.*, 35, 1712–1725, 1978.

Davies, R., Documentation of the solar radiation parameterization in the GLAS climate model, *NASA Tech. Memo., 83961*, 57 pp., 1982.

Frouin, R., and B. Chertock, A technique for global monitoring of net solar irradiance at the ocean surface, I, Model, *J. Appl. Meteorol.*, 31, 1056–1066, 1992.

Geleyn, J. F., and A. Hollingsworth, An economical analytical method for the computation of the interaction between scattering and line absorption of radiation, *Beitr. Phys. Atmos.*, 52, 1–16, 1979.

Geleyn, J. F., A. Hense, and H. J. Preuss, A comparison of model generated radiation fields with satellite measurements, *Beitr. Phys. Atmos.*, 55, 253–286, 1982.

Harshvardhan, The effect of brokenness on cloud-climate sensitivity, *J. Atmos. Sci.*, 39, 1853–1861, 1982.

Harshvardhan, R. Davies, D. A. Randall, and T. G. Corsetti, A fast radiation parameterization for atmospheric circulation models, *J. Geophys. Res.*, 92, 1009–1016, 1987.

Harshvardhan, D. A. Randall, T. G. Corsetti, and D. A. Dazlich, Earth radiation budget and cloudiness simulations with a general circulation model, *J. Atmos. Sci.*, 46, 1922–1942, 1989.

Hartmann, D. L., M. E. Ockert-Bell, and M. L. Michelsen, The effect of cloud type on Earth's energy balance: Global analysis, *J. Clim.*, 5, 1281–1304, 1992.

Heymsfield, A. J., and R. G. Knollenberg, Properties of cirrus generating cells, *J. Atmos. Sci.*, 29, 1358–1366, 1972.

Heymsfield, A. J., and C. M. R. Platt, A parameterization of the particle size spectrum of ice clouds in terms of the ambient temperature and the ice water content, *J. Atmos. Sci.*, 41, 846–855, 1984.

Hogan, T. F., and L. R. Brody, Sensitivity studies of the Navy's Global Forecast Model parameterizations and evaluation of improvements to NOGAPS, *Mon. Weather Rev.*, 121, 2373–2395, 1993.

Hogan, T. F., and T. E. Rosmond, The description of the Navy Operational Global Atmospheric Prediction System's Spectral Forecast Model, *Mon. Weather Rev.*, 119, 1786–1815, 1991.

Jacobowitz, H., H. V. Soule, H. L. Kyle, F. B. House, and the Nimbus-7 ERB Experiment Team, The Earth Radiation Budget (ERB) Experiment: An overview, *J. Geophys. Res.*, 89, 5021–5038, 1984.

Kiehl, J. T., and V. Ramanathan, Comparison of cloud forcing derived from the Earth Radiation Budget Experiment with that simulated by the NCAR community climate model, *J. Geophys. Res.*, 95, 11,679–11,698, 1990.

Kite, A., The albedo of broken cloud fields, *Q. J. R. Meteorol. Soc.*, 113, 517–531, 1987.

Kyle, H. L., P. E. Ardanuy, and E. J. Hurley, The status of the Nimbus-7 Earth Radiation Budget data set, *Bull. Am. Meteorol. Soc.*, 66, 1378–1388, 1985.

Kyle, H. L., A. Mecherikunnel, P. Ardanuy, L. Penn, B. Groveman, G. G. Campbell, and T. H. Vonder Haar, A comparison of two major Earth Radiation Budget data sets, *J. Geophys. Res.*, 95, 9951–9970, 1990.

Lacis, A. A., and J. E. Hansen, A parameterization for the absorption of solar radiation in the Earth's atmosphere, *J. Atmos. Sci.*, 31, 118–133, 1974.

Laszlo, I., and R. T. Pinker, Shortwave cloud-radiative forcing at the top of the atmosphere at the surface and of the atmospheric column as determined from ISCCP C1 data, *J. Geophys. Res.*, 98, 2703–2713, 1993.

Liou, K. N., Influence of cirrus clouds on weather and climate processes: A global perspective, *Mon. Weather Rev.*, 114, 1167–1199, 1986.

Liou, K. N., J. L. Lee, S. C. Ou, Q. Fu, and Y. Takano, Ice cloud microphysics, radiative transfer and large-scale cloud processes, *Meteorol. Atmos. Phys.*, 46, 41–50, 1991.

London, J., A study of the atmospheric heat balance, *Final Rep. AFC-TR-57-287, OTSPB129551*, 99 pp., Coll. of Eng., New York Univ., New York, 1957.

McKee, T. B., and S. K. Cox, Scattering of visible radiation by finite clouds, *J. Atmos. Sci., 31*, 1885–1892, 1974.

Morcrette, J.-J., Impact of changes to the radiation transfer parameterizations plus cloud optical properties in the ECMWF model, *Mon. Weather Rev., 118*, 847–873, 1990.

Ockert-Bell, M. E., and D. L. Hartmann, The effect of cloud type on earth's energy balance: Results for selected regions, *J. Clim., 5*, 1157–1171, 1992.

Ohring, G., and P. F. Clapp, The effect of changes in cloud amount on the net radiation at the top of the atmosphere, *J. Atmos. Sci., 37*, 447–454, 1980.

Potter, G. L., J. M. Slingo, J.-J. Morcrette, and L. Corsetti, A modeling perspective on cloud radiative forcing, *J. Geophys. Res., 97*, 20,507–20,518, 1992.

Ramanathan, V., R. D. Cess, E. F. Harrison, P. Minnis, B. R. Barkstrom, E. Ahmad, and D. Hartmann, Cloud-radiative forcing and climate: Results from the Earth Radiation Budget Experiment, *Science, 243*, 57–63, 1989.

Randall, D. A., Harshvardhan, D. A. Dazlich, and T. G. Corsetti, Interactions among radiation, convection, and large-scale dynamics in a general circulation model, *J. Atmos. Sci., 46*, 1943–1970, 1989.

Ritter, B., and J. F. Geleyn, A comprehensive radiation scheme for numerical weather prediction models with potential applications in climate simulations, *Mon. Weather Rev., 120*, 303–325, 1992.

Slingo, J., The development and verification of a cloud prediction scheme for the ECMWF model, *Q. J. R. Meteorol. Soc., 113*, 899–927, 1987.

Slingo, A., and H. M. Schrecker, On the shortwave radiative properties of stratiform water clouds, *Q. J. R. Meteorol. Soc., 108*, 407–426, 1982.

Slingo, A., and J. M. Slingo, The response of a general circulation model to cloud longwave radiative forcing, I, Introduction and initial experiments, *Q. J. R. Meteorol. Soc., 114*, 1027–1062, 1988.

Slingo, A., and J. M. Slingo, Response of the National Center for Atmospheric Research Community Climate Model to improvements in the representation of clouds, *J. Geophys. Res., 96*, 15,341–15,357, 1991.

Slingo, A., R. C. Wilderspin, and S. J. Brentnall, Simulation of the diurnal cycle of outgoing longwave radiation with an atmospheric GCM, *Mon. Weather Rev., 115*, 1451–1457, 1987.

Smith, L. D., and T. H. Vonder Haar, Clouds-radiation interactions in a general circulation model: Impact upon the planetary radiation balance, *J. Geophys. Res., 96*, 893–914, 1991.

Smith, R. N. B., A scheme for predicting layer cloud and their water content in a general circulation model, *Q. J. R. Meteorol. Soc., 116*, 435–460, 1990.

Soden, B. J., Validation of cloud forcing simulated by the National Center For Atmospheric Research Community Climate Model using observations from the Earth Radiation Budget Experiment, *J. Geophys. Res., 97*, 18,137–18,159, 1992.

Stephens, G. L., Radiation profiles in extended water clouds, II, Parameterization schemes, *J. Atmos. Sci., 35*, 2123–2132, 1978a.

Stephens, G. L., Radiation profiles in extended water clouds, I, Theory, *J. Atmos. Sci., 35*, 2111–2122, 1978b.

Stephens, G. L., and S.-C. Tsay, On the cloud absorption anomaly, *Q. J. R. Meteorol. Soc., 116*, 671–704, 1990.

Tian, L., and J. A. Curry, Cloud overlap statistics, *J. Geophys. Res., 94*, 9925–9935, 1989.

Vesperini, M., J.-J. Morcrette, and Y. Fouquart, Simulation of cloud radiative forcing with the ECMWF model, *Dyn. Atmos. Oceans, 16*, 85–109, 1991.

Warner, J., The water content of cumuliform cloud, *Tellus, 7*, 449–457, 1955.

Warner, J., The microstructure of cumulus cloud, I, General features of the droplet spectrum, *J. Atmos. Sci., 26*, 1049–1059, 1969.

Weinman, J. A., and Harshvardhan, Solar reflection from a regular array of horizontally finite clouds, *Appl. Opt., 21*, 2940–2944, 1982.

Welch, R. M., and B. A. Wielicki, Stratocumulus cloud field reflected fluxes: The effect of cloud shape, *J. Atmos. Sci., 41*, 3085–3103, 1984.

Wiscombe, W. J., R. M. Welch, and W. D. Hall, The effects of very large drops on cloud absorption, I, Parcel models, *J. Atmos. Sci., 41*, 1336–1355, 1984.

B. Chertock, NOAA Environmental Technology Laboratory, 325 Broadway, Boulder, CO 80303.

R. Gelaro and J. A. Ridout, Naval Research Laboratory, 7 Grace Hopper Ave., Box 2, Monterey, CA 93943-5502.